

Estimating regional effects of climate change and altered land use on biosphere carbon fluxes using distributed time delay neural networks with Bayesian regularized learning

Andres Schmidt^{a,*}, Whitney Creason^b, Beverly E. Law^b

^a RWTH Aachen University, Department of Geography, 52062 Aachen, Germany

^b Oregon State University, Department of Forest Ecosystems and Society, Corvallis, OR 97331, USA

ARTICLE INFO

Article history:

Received 6 April 2018

Received in revised form 18 June 2018

Accepted 2 August 2018

Available online 16 August 2018

Keywords:

Distributed time delay neural networks

Bayesian learning

Climate change

Atmospheric carbon exchange modeling

ABSTRACT

The ability to accurately predict changes of the carbon and energy balance on a regional scale is of great importance for assessing the effect of land use changes on carbon sequestration under future climate conditions. Here, a suite of land cover-specific Distributed Time Delay Neural Networks with a parameter adoption algorithm optimized through Bayesian regularization was used to model the statewide atmospheric exchange of CO₂, water vapor, and energy in Oregon with its strong spatial gradients of climate and land cover. The network models were trained with eddy covariance data from 9 atmospheric flux towers. Compared to results derived with more common regression networks utilizing non-delayed input vectors, the performance of the DTDNN models was significantly improved with an average increase of the coefficients of determination of 64%.

The optimized models were applied in combination with downscaled climate projections of the CMIP5 project to calculate future changes in the cycle of carbon, associated with a prescribed conversion of conventional grass-crops to hybrid poplar plantations for biofuel production in Oregon. The results show that under future RCP8.5 climate conditions the total statewide NEP increases by 0.87 TgC per decade until 2050 without any land use changes. With all non-forage grass completely converted to hybrid poplar the NEP averages 32.9 TgC in 2046–2050, an increase of 9%. Through comparisons with the results of a Bayesian inversion study, the results presented demonstrate that DTDNN models are a specifically well-suited approach to use the available data from flux networks to assess changes in biosphere–atmosphere exchange triggered by massive land use conversion superimposed on a changing climate.

© 2018 Elsevier Ltd. All rights reserved.

1. Introduction

The accurate spatiotemporal quantification of the exchange of carbon, water, and energy between the land surface and the atmosphere using measurements, remote sensing products, or models is of vital importance to understand the processes involved and subsequently simulate them in mechanistic earth-system models in an adequate and sufficiently detailed manner. While eddy covariance (EC) measurements are the only direct method to quantify turbulent vertical exchange of airborne constituents and energy (Wyngaard, 1990), EC measurements can only capture exchange rates on a spatially limited, micrometeorological level of several hundred meters (up to several kilometers at nighttime) that define the footprint of the tower, depending on meteorological conditions, roughness, and measurement height above the surface or

canopy, respectively (e.g. Baldocchi et al., 2001; Schuepp, Leclerc, MacPherson, & Desjardins, 1990).

To date, EC towers are too sparsely distributed for assessments beyond the local scale or the maximum scale over which the homogeneity of the surface properties represented by the tower footprint extend. Thus, in order to calculate the biosphere–atmosphere exchange on a larger scale, models are needed. These models are often driven by data from remote-sensing products or gridded reanalysis climate data to facilitate analyses on regional to global scales (e.g. Ito, Inatomi, Huntzinger, Schwalm, Michalak, et al., 2016; Schmidt et al., 2016; Welp et al., 2016).

While diagnostically powerful, the predictive capability of mechanistic vegetation process model simulations is confined by a static process model structure and the burden of model-specific parameterization. Often perplexing associations between observed ecosystem carbon flux and its physical drivers make a quantitative assessment of their linkages difficult (Stoy et al., 2005) leading to incomplete or crude mathematical formulations of the system. Machine learning approaches, specifically neural network

* Corresponding author at: RWTH Aachen University, Department of Geography, 52062 Aachen, Germany.

E-mail address: andres.schmidt@geo.rwth-aachen.de (A. Schmidt).

models, are an alternative method to model biosphere fluxes. Generally, artificial neural networks (ANNs) are a strictly data-driven machine learning approach that iteratively learns the functional dependencies between driving variables and target variables of interest in a supervised or unsupervised manner (e.g. Bishop, 2006; Haykin, 1998, 2009). The advantage of a neural network model over a mechanistic process model is that no prior knowledge about functional relationships between the driving input variables and the target variable is needed. Thus, no model-simplifications that constrain the outcome by the number of available algorithms and corresponding parameterization are required.

The downside, however, is that no functions can be derived that allow the exploration of physical relations between drivers and response in a post analysis. Instead, the input vectors are mathematically mapped on the training targets by iterative function parameter approximation and error minimization, regardless of any physical processes that explain the observations of the drivers and the output variables of interest. This purely mathematical approximation approach leads to complex combinations of many functions that allow mapping the inputs on the target variable. Nevertheless, those functions are ill-suited for a direct exploration of the underlying physical processes such as edaphic processes or plant physiological limitations when biosphere–atmosphere exchange is analyzed.

Despite the shortcomings in terms of explanatory algorithms, ANNs have been successfully used in previous surface–atmosphere exchange studies to analyze patterns fluxes or to fill gaps in corresponding observational data (e.g. Dengel et al., 2013; Menzer, Meiring, & Kyriakidis, 2015; Papale & Valentini, 2003; Schmidt, Wrzesinsky, & Klemm, 2008; Schmidt, Hanson, Kathilankal, & Law, 2011).

Here, we present an approach to model the turbulent surface–atmosphere exchange of CO_2 over Oregon using Distributed Time Delay Neural Networks (DTDNN). First introduced by Waibel, Hanazawa, Hinton, Shikano, and Lang (1989), time delay neural networks are a class of neural networks specifically suitable for time series analyses. Unlike regular feed forward regression networks, time delay networks not only apply an input vector to estimate a temporally corresponding output value, but use additional information from previous time steps in the form of time series sequences of input vectors (Haykin, 2009; Liu, Wang, & Liu, 2006; Peddinti, Povey, & Khudanpur, 2015; Wang, Liu, & Liu, 2005). By using this temporally accrued input of driver variables these models implement the mathematical approximation of accumulation and delayed processes on the output (e.g. Liu, Wang, Liang, & Liu, 2008; Rahman, Blyuss, & Krychko, 2015; Waibel et al., 1989).

Measured atmospheric fluxes and net radiation time series from 9 eddy covariance towers were used to train and validate specific DTDNN models for 9 different land use and land cover (LULC) types that are dominant in our study domain which covers the state of Oregon in the Pacific Northwest. The DTDNN models are driven using downscaled reanalysis climate variables of the METDATA dataset (Abatzoglou, 2013) to reproduce net ecosystem exchange of CO_2 (NEE) and the corresponding annual net ecosystem production (NEP).

To reproduce measured NEE and subsequently model future NEE we also trained specific networks to model sensible heat flux (H), latent heat flux (LE), and net radiation (R_{net}). The modeled heat fluxes and R_{net} were then used as additional important input variables for the LULC specific NEE models.

We applied our models in conjunction with downscaled ($1/24^\circ$ -grid, 3-hourly) climate projection data of the CMIP5 project (Taylor, Stouffer, & Meehl, 2012) to estimate future changes in the carbon cycle associated with LULC conversion under future climate conditions (Section 2.2).

Other studies on the influence of land management and harvesting practices in Oregon found significant impacts on the carbon

cycle, especially when LULC changes are superimposed on a changing climate (e.g. Creutzburg et al., 2016; Dempsey et al., 2017; Hudiburg, Luyssaert, Thornton, & Law, 2013). The transferability of the results found in those important studies is, however limited because of either a coarse spatial and temporal resolution of the mechanistic models or because the studies focused only on small distinct areas or specific ecosystems.

With its spatial climate gradient and heterogeneous LULC (Turner et al., 2007) Oregon offers a specifically interesting case to examine the effect of LULC change in support of bioenergy production superimposed on the effects of climate change on the biosphere–atmosphere exchange. The Boardman power facility is the only coal-fired plant in Oregon. Its emissions are 2.3 Mt per year, making it the largest single source of anthropogenic CO_2 emissions in the state (OGWC, 2017). It is located in the semi-arid region of the Columbia Plateau (Fig. 1). To meet the state's greenhouse gas emissions reduction goal, the process of switching this power plant from coal combustion to bioenergy or other alternative energy source must be completed by the end of 2020.

In this study we examine the atmospheric exchange of carbon, water, and energy when crop land is converted to bioenergy plantations to meet those requirements in the state of Oregon. In particular, non-forage grass crops are converted into hybrid poplar plantations using 3 different scenarios exhibiting distinct rates of conversion.

To distinguish between the effects of changing climate conditions and LULC change, the results for the three conversion rate scenarios are compared to a business as usual (BAU) scenario with no land use changes prescribed. We present future estimates of statewide NEP and energy exchange by combining an advanced machine learning approach with a rich dataset of flux measurements and downscaled climate data.

2. Data and methods

2.1. Flux tower sites and data

The flux data to train each specific network model are from 9 AmeriFlux sites that are equipped with EC systems and standard meteorological sensors for measurements of air temperature, relative humidity and wind, as well as net radiometers and sensors for photosynthetically active radiation. The AmeriFlux network conducts rigorous quality control of the measurements and the data provided which makes the database a suitable source for model development and verification (Baldocchi, 2003; Schmidt, Hanson, Chan, & Law, 2012). The EC fluxes used in this study were calculated based on 20 Hz measurements of wind components and gas concentration or mixing ratios, respectively. For the measurements conducted with open-path infrared gas analyzers (LICOR LI-7500), the half-hourly flux values were corrected for density fluctuations (WPL) (Webb, Pearman, & Leuning, 1980). For the closed-path measurements (LICOR LI-7200 and PICARRO CFBDS2020), the mixing ratio was applied directly (Burba et al., 2011). Net radiation at the flux sites was derived from measurements using Kipp & Zonen CNR1 or Hukseflux NR01 net Radiometers, respectively. A summary of the flux site instrumentation used in the data for this study is given in Table 1.

For the model training, 3-hourly averages were used to reduce the effect of noisy flux data on the development of the generalization models while still capturing the sub-daily fluctuations of physiological plant responses and respective flux driving meteorological variables. Using long-term datasets in sub-daily temporal resolution ensures the models are exposed to a wide scale of values during the learning process. If the long-term average temperature increases when future climate scenarios are considered, the 3-hourly data of the climate predictions will unlikely be outside of

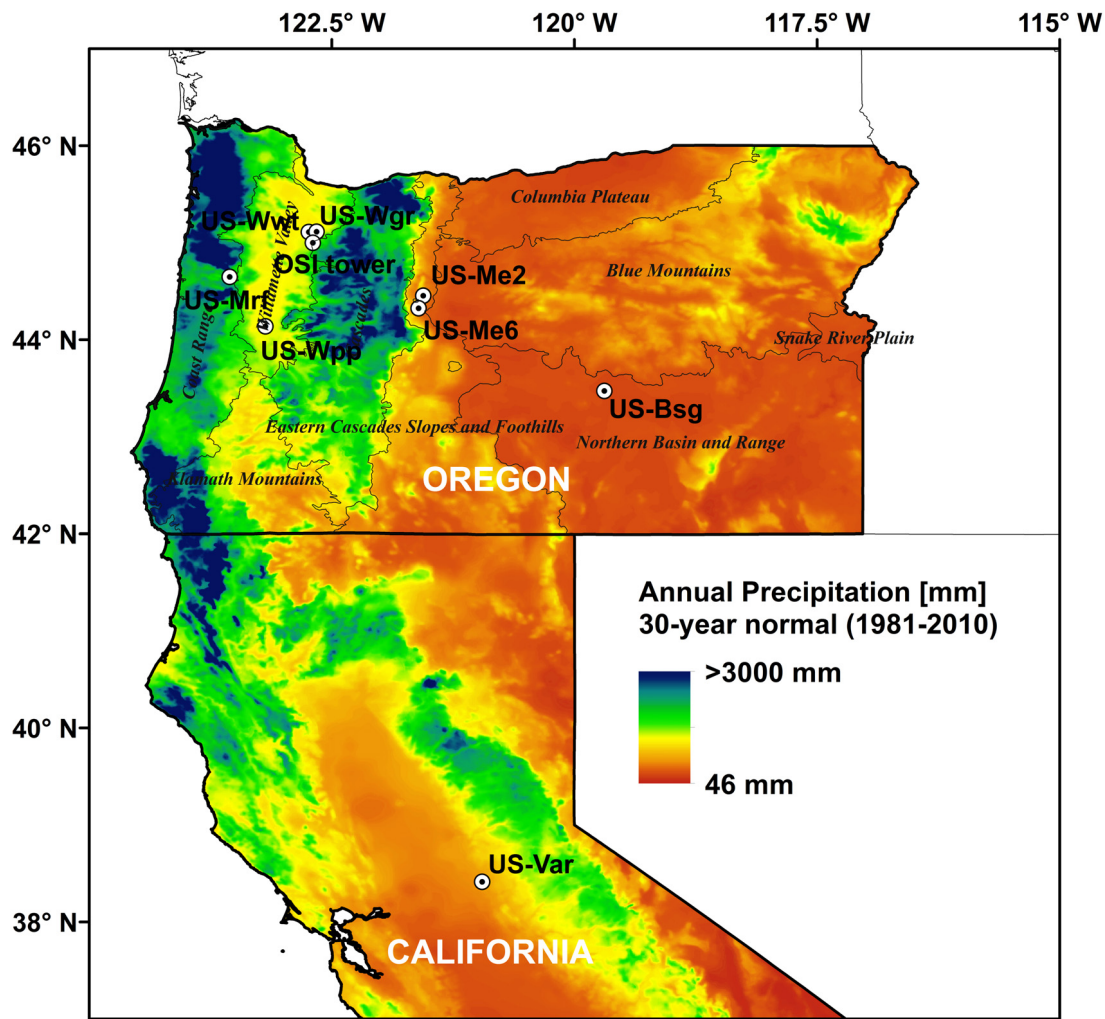


Fig. 1. 30-year normal of precipitation from the 800 m resolution PRISM data for Oregon and North-California. The color marking shows the strong west–east climate gradient in Oregon and the similarity of the precipitation regime at the California site used to represent grassland fluxes in northeast Oregon. The markers show the locations of the EC flux towers used to train the neural networks. The distinct Level III ecoregions of Oregon (Omernik, 1995; Thorson et al., 2003) are outlined in gray.

Table 1

Flux tower sites providing the measured data for the model training and evaluation processes.

Tower ID	Ecoregion/LULC class	Average height of vegetation (m)	Latitude	Longitude	Elevation (m a.s.l.)	Measurement heights (m a.g.l.)	EC and RN instrumentation
US-Me2	Eastern Cascades and Foothills/mature pine forest	19	44.4524	−121.5572	1253	36	CSAT3+LI-7200/7500/CNR1
US-Me6	Eastern Cascades and Foothills/young pine forest	7.5	44.3228	−121.6047	998	15	CSAT3+LI-7200/7500/CNR1
US-Bsg	Northern Basin and Range/brush and grassland	1.2	43.4712	−119.6909	1398	20	CSAT3+LI-7200/CNR1
US-Wwt	Willamette Valley/winter wheat and spring wheat	0.8	45.1089	−122.6664	52	2.5	CSAT3+LI-7500/CNR1
US-Wgr	Willamette Valley/Grass-crops	0.4	45.1126	−122.6561	52	2.5	CSAT3+LI-7500/ CNR1
OSI	Willamette Valley/Other crops	0.3	44.9986	−122.6948	351	5	CSAT3+CRDS/CNR1
US-MRf	Coast Range Mountains/Douglas fir forest	27	44.6465	−123.5514	263	36	CSAT3+LI-7500, CNR1
US-Var	Central California Chaparral and Oak Woodlands/C3 grasses	0.3	38.4133	−120.9507	129	1.7	Gill WM 1590+ LI-7500/CNR1
US-Wpp	Southern Willamette Valley/Poplar	16.2	44.13685	−123.1824	111	18	CSAT3+LI-7500/ CNR1

the range with which the networks were trained. Thus, our models trained with meteorological data and flux data from up to 12 years back to very recent years (2014 to 2015) will produce meaningful fluxes and net radiation values when applied with future climate data.

The 9 flux sites used for our DTDNN development are well distributed and cover the most dominant vegetation land covers (natural vegetation and crops) needed to represent the types used for our LULC classification (Table 1). The flux sites also represent the strong climate gradient found in our study domain. In Fig. 1

the average precipitation is given using the 800 m resolution data from the Parameter-elevation Relationships on Independent Slopes Model (PRISM) (Daly et al., 2008). The strong east–west gradient induced by the topographic features in Oregon is clearly visible reaching from less than 100 mm precipitation per year in the east of the state to over 4500 mm in some areas in the northwest of Oregon for the 30-year normal.

The major agricultural crops in Oregon are winter and spring wheat (360,000 ha), alfalfa hay (155,000 ha) and grass seed (145,000 ha) (USDA, 2014). The wheat and grass crops in this study were represented by the AmeriFlux sites US-Wgr and US-Wwt, respectively.

The grass crop site (US-Wgr) is in the northern Willamette Valley near Molalla, OR. Measurements were conducted from 2014–2016 over perennial tall fescue (*Festuca arundinacea*) that is a major crop in the Valley and harvested once per year.

The agricultural wheat site (US-Wwt) is also in the northern Willamette Valley near Molalla, OR. Between 2014 and 2016, crops were rotated between winter wheat (*Triticum aestivum*) and spring wheat planted in adjacent fields. Measurements were made in one of the two fields, depending on the season. The US-Wwt and the US-Wgr sites were both equipped with the former AmeriFlux QA/QC lab mobile reference systems as described in detail in Schmidt et al. (2012).

Model development for Oregon's non-agricultural grasslands relies on data from the AmeriFlux Vaira Ranch grassland site (US-Var) in California. The site is lightly used for grazing (Peichl et al., 2013) and the climate conditions are comparable to grasslands in Oregon's dry ecoregions. Natural grassland is abundant in the Columbia Basin in Northeast Oregon and the Northern Great Basin in Southeast Oregon. The NEP of C3 grassland sites with various species mostly differs because of climate conditions (air temperature, precipitation, and soil moisture) rather than species composition (Peichl et al., 2013; Wagle et al., 2015). Although the US-Var site is composed of different species than Oregon, the fluxes are considered representative of the study area.

The poplar site (US-Wpp) is part of a bioenergy project operated by the cities of Eugene and Springfield in the southern Willamette Valley. The trees were planted in 3 phases beginning spring 2004, 2007, and 2009. There are approximately 162 hectares of hybrid poplar. *Populus trichocarpa* × *deltoids* is the dominant species. The mean canopy height is 16.2 m adjacent to the tower, maximum LAI is 3.90 m² m⁻², and stand density is 636 trees ha⁻¹ as of 2015.

The long-term core AmeriFlux site (US-Me2) is located within a mature ponderosa pine forest in the East Cascades ecoregion in the rain shadow of the Cascade Mountains (Fig. 1). The data from this site was used to represent mature pine forests, abundant especially in the eastern slopes of the Cascade Mountains. The climate at the flux site is characterized by warm, dry summers and cool, wet winters. Most precipitation occurs from November through April (Schwarz et al., 2004), with the mean annual temperature 6.28 °C and mean annual precipitation 523 mm.

The site is a mixed-age stand consisting of predominately ponderosa pine (*Pinus ponderosa*) interspersed with grand fir (*Abies grandis*) and incense cedar (*Calocedrus decurrens*). The summer maximum LAI is 2.6 m² m⁻² as of 2015. The understory consists of greenleaf manzanita (*Arctostaphylos patula*), and antelope bitterbrush (*Purshia tridentata*) with an understory LAI of 0.66 m²/m². In 2015, the mean stand age was 69 years (oldest 10% of trees 106 years), mean tree height 19 m, and stand density 339 trees ha⁻¹. A more detailed description of the site location and EC instrumentation can be found in Vickers, Thomas, Pettijohn, Martin, and Law (2012).

The young pine site US-Me6 (Fig. 1) is located 15 km south-southwest of the US-Me2 site. While the site is also located at the Eastern slopes of the Cascade Mountains in the same ecoregion, the

stand is more open and significantly younger than US-Me2 with an average age of 22 years and an average tree height of 7.5 m. The overstory is exclusively ponderosa pine with a maximum LAI of 1.38 m² m⁻² and a stand density of 140 trees ha⁻¹.

The mature Douglas fir site US-Mrf was located on the east side of the Coast mountain range, near Summit, OR. The mean annual temperature is 10.2 °C and the mean annual precipitation is 1820 mm. The overstory is predominately Douglas fir (*Pseudotsuga menziesii*) with a maximum LAI of 8.11 m² m⁻². The mean tree height is 31.2 m and tree density is about 414 trees ha⁻¹. Mean stand age is 51 years, as of 2015. The understory coverage is 90% salal (*Gaultheria shallon*).

The US-Bsg sagebrush site is located in the Oregon high desert, about 60 km southwest of Burns, OR. The vegetation is predominately big sagebrush (*Artemisia tridentata*) with rabbit brush (*Chrysothamnus* spp.) and bunchgrasses (*Festuca* spp.) sparsely interspersed. Further details about the US-Bsg site can be found in Schmidt et al. (2016).

The OSI site is located on the east side of the Willamette Valley (Fig. 1). The measurement height of the EC system is 5 m above ground. The annually rotated crops around the tower are vetch (*Vicia* spp.), a variety of perennial flowers for seed production, and canola. The flux data was applied to represent the variety of agricultural, non-wheat and non-grass sites found in Oregon and binned as 'other crops' in our LULC classification (Table 1).

2.2. Climate driver data

For the training procedure of each DTDNN model we used the gridded METDATA dataset to provide meteorological inputs. This daily surface reanalysis dataset covers the period from 1979 to current with 1/24° spatial resolution. The dataset provides gridded climate variables for the contiguous USA that were thoroughly validated against a large number of meteorological observations (Abatzoglou, 2013). To train the networks for sub-daily resolution of fluxes and net radiation, all values from the METDATA source data were temporally downsampled to 3-hourly averages or sums (precipitation). As climate data input for the network models for the predictive runs we used gridded global climate model (GCM) data that was downsampled to a horizontal resolution of 1/24 degree (approximately 4 x 4 km in our study area) and 3-hourly temporal resolution. The climate driver variables we used are air temperature (T_{air}), incoming shortwave radiation (RSW), precipitation (P), specific humidity (SH) (all measurements near surface at 2 m above ground), and wind velocity at 10 m above ground (U).

For the future model runs projections to 2050, CMIP5 climate projections were statistically downsampled and bias corrected using the Multivariate Adaptive Constructed Analogs method (MACA) (Abatzoglou & Brown, 2012). We used the MIROC5 RCP8.5 GCM results as climate input for the future DTDNN model runs. Further details about the temporal and spatial scaling of the climate input for the model training procedures can be found in Schmidt et al. (2016) and in Appendix A.

To relate the changes of future biosphere–atmosphere exchanges to the climate drivers we calculated the seasonal anomalies for the 3 most important climate variables for each level III ecoregion. To assess the future changing conditions based on our climate input data, we calculated seasonal anomalies for 4 decades using the climate averages from 1981 to 2010 as reference period. The analyses were conducted for individual ecoregions to allow an improved visualization of the spatially distinctive changes to each level III region (Fig. 1), characterized by its distinct climate, soil and vegetation cover.

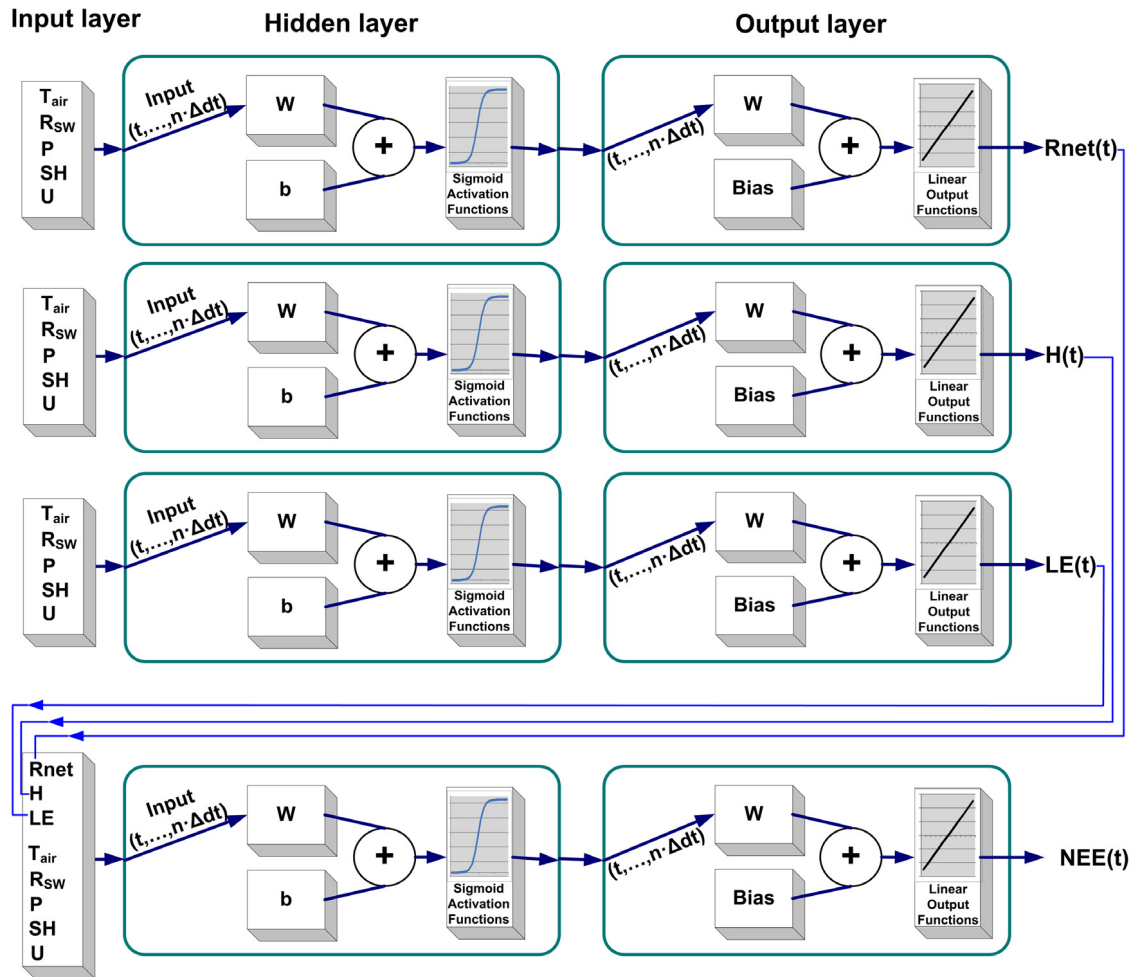


Fig. 2. Schematic of the DTDNN model setup. Time series segments ($t - n \cdot \Delta t$) of each input vector are applied on the neuron weights (w) through the tap delay line in the input layer and the output neuron layer. This way the accumulated effect of the input variables $x(t)$ over a period of n time steps on the output at time t can be accounted for by the DTDNN models. The gridded time series modeled for R_{net} , H , and LE are used as additional network input for the target variable NEE in the subsequent modeling step.

2.3. Distributed time delay neural network models

Feed-forward networks using classical topologies, for example, multilayer perceptron and radial basis function networks (e.g. Bishop, 2006) have been successfully used in previous studies to either analyze patterns of surface–atmosphere exchange of carbon, water, and energy or to fill gaps in flux data using climate variables as input (e.g. Dengel et al., 2013; Papale & Valentini, 2003; Menzer et al., 2015; Schmidt et al., 2008; Schmidt et al., 2011).

In this study we apply a neural network approach capable of taking into account time shifts between driving variables and associated responses of the vegetation. The additional delayed input line connected to the weights of the networks nodes allow time delay networks (e.g. Haykin, 1998; Haykin, 2009) to have a dynamic response to time series input data (Fig. 2).

The inherent memory and implementation of previous states by this specific network type enable the DTDNN models to account for various lags between environmental conditions (causes) and ecosystem functions (effects) such as the uptake or release of CO_2 or water vapor. Turbulent fluxes above ecosystems are affected through several time delays in the response of the plants to changing meteorological conditions.

The enhanced release of water through the stomata in response to precipitation, for instance, is delayed because the water, once it has reached the soil, has to be taken up and transported through the plant. Depending on plant type, individual plant height, and

environmental conditions, the transport process can take from less than an hour up to several days and even weeks in tall trees (Gaines, Meinzer, Duffy, Thomas, & Eissenstat, 2016; Meinzer et al., 2006). However, since water is stored in the stem tissue of taller trees and the transpiration is controlled by the stomata, evaporation measured above the canopy can change long before the exact same water molecules originating from a distinct measured precipitation event reach the leaves. These control mechanisms lead to various delays between water uptake after an observed rain event and the associated measurable change in evaporation (LE). If a static network or any type of a regression model is trained to quantify those processes by directly modeling the response functions using only temporally corresponding driving variables, the delays unaccounted for lead to reduced model performance.

While a coarse temporal resolution will allow for mathematically associations between meteorological or climate conditions and plant responses like flux rates, the precision of the results is limited by the remaining correlation of the inputs and corresponding response measures.

Shifting the time series manually would require the exact knowledge of the delays between cause and measurable effect for each driver. Data must also be available in sufficient temporal resolution to resolve the duration of the respective processes to be modeled. Recognition of temporal patterns and dependencies requires processing of patterns that develop over time and produce a response at a certain time which not only depends on the

contemporaneous input values but also on the past state of the system that describes the input-space. Thus, the processes that lead to a distinct ecosystem response observed at a given time can be presented to the learning model more realistically by also incorporating past driving inputs such as the fluctuations in air temperature or the amount of radiation. When considering time series versus only contemporary vectors of input variables, the significant increase in performance can be attributed to the fact, that for the variables modeled, delays between the direct meteorological/climate input and the physical (Rnet, H) and physiological (NEE, LE) responses are to be expected. As an example, one could compare two different situations, assuming no water or nutrient limitations in both cases. First, we assume overcast conditions with low direct down-welling shortwave radiation including the photosynthetically active wavelength spectrum. If the cloud cover opens and the amount of direct (and diffuse) radiation changes, a corresponding change in photosynthesis and associated CO₂ uptake will occur. The strength of CO₂ uptake (or latent heat flux) briefly after the altered cloud cover will be different from the uptake that one would measure if there was no cloud cover at all during the previous hours. Factors driving CO₂ uptake such as leaf temperature and water conductance will be different in both radiation situations. Thus, the fluxes of heat, water and CO₂ at time t depend on the conditions accumulated during a preceding time period, rather than only on the present conditions with no delay considered. This memory effect plays a particularly significant role when biosphere processes are to be derived from driver variables used as model input. Since the DTDNNs use the inherent dependability of the output on a previous consecutive time series of input variables we used only continuous data segments for the network model training.

Since the training target data consists of tower measurements, data gaps are inevitable. Especially the EC data of atmospheric fluxes can hardly ever be without gaps over long periods of several month or years as used here, due to the theoretical requirements and deployed measurement devices. Thus, if a training data series was interrupted, the training was stopped and the network trained thus far was saved. Then the network was re-trained with the next available continuous data section until all available sections assigned to the training data subset were utilized.

This method enabled us to train the networks appropriately for the time delay approach providing all input variables at all backward time steps considered to produce the target value at a distinct time.

The DTDNN approach differs from existing efforts to model plant response to climate change in that we can fully capitalize on the data's temporal information content. That is, the lags, cumulative thresholds, switches, and hysteresis that so complicate mechanistic modeling approaches are systematically evaluated through the delay network algorithm.

For the field crops that were harvested once a year during the study period, we added a Boolean harvest variable as model input to temporarily segregate the data sections for the calculations. Since the fluxes and R_{net} values change drastically after the crop fields are harvested, the additional binary variable (1 for pre-harvest conditions and 0 for post-harvest conditions) accounts for the correspondingly strong and sudden change of functional relation between the climate input, the fluxes, and R_{net} .

2.3.1. Bayesian regularization for network model training

We used a Bayesian regularization technique to optimize the parameterization of each DTDNN (Burden & Winkler, 2009; Foresee & Hagan, 1997; Močkus, Tiesis, & Zilinskas, 1978). Here, we provide a brief introduction to the neural network learning process, in general, and Bayesian regularization, in particular as an important basis of our method. Details about neural networks and training

algorithms can be found in the respective literature (e.g. Haykin, 1999; Bishop, 2006; Haykin, 2009). In order to iteratively adjust the parameters of a neural network (i.e., weights \mathbf{w} and biases \mathbf{b} of the neuron connections) the available dataset consisting of the input vector and the corresponding targets is subdivided into the training data, the validation data, and the test dataset. The training data is used to present the data to the new network. Once the output is modeled the parameters of the network are adjusted based on the obtained error, i.e. the difference between the training target and the model output (Eq. (1)).

Once an acceptable difference between the network output and the available known target values is achieved the validation dataset is presented to the network. Since the validation dataset has not been used for the adjustment of the parameters the validation data can be considered new data. Hence, an increasing validation error indicates that network parameters (i.e. the network weight vectors \mathbf{w} and biases \mathbf{b}) are over-adjusted to the available training data including the statistical noise in the data. In that case, the network parameters are optimized to reproduce the training examples. However, the network is unable to accurately generalize the functional relationship between the inputs and target outputs and the data. This produces unsuitable outputs when confronted with new data not involved during the training procedure. Thus, during a common back propagation learning procedure the adjustment of the network parameters is stopped at an optimum between the training error and the validation error once the validation error starts increasing (e.g. Schmidt et al., 2008). The final portion of the learning dataset, the test data, was not used during the training and validation procedure. Therefore it is applicable to assess the performance of the network when confronted with new data. Thus, the test error quantifies the actual performance of the final network.

For Bayesian regularization, no validation data is used but only the training data and the test data subsets are required. Eliminating the need for a validation data subsample leaves more training data, which is an additional advantage over the cross-validation approach if the available learning dataset is limited. The regularization approach involves modifying the performance or error function. The problem of regular optimization procedure is that in order to achieve a small enough error, the weights of a neural network are often over-adjusted to the training data. This happens, in particular, if random noise or outliers remain in the data available for the learning procedure. This is associated with large values of the network weights. To address this unwanted adjustment effect, the performance function of the network (usually the MSE, Eq. (1)) is modified. In particular, the error function is enhanced to search for the minimal error using minimal weights.

$$E = \frac{1}{N} \sum_{i=1}^N (m_i - o_i)^2 \quad (1)$$

Here, o_i are the observed target values of the i training cases presented to the network and m_i are the corresponding outputs modeled by the network.

To incorporate the number and sum of weights as an optimization goal, a term is added to the error function to quantify the mean of the sum of squares of the network weights E_w (Eq. (2)). This leads to a weighted error function, or cost function F , as given in Eq. (3). Here, w_j is the j th element of the weight vector \mathbf{w} of length n . α and β are performance function weight parameters between 0 and 1.

$$E_w = \frac{1}{n} \sum_{j=1}^n w_j^2 \quad (2)$$

$$F = \alpha E_w + \beta E, \text{ with } \alpha + \beta = 1 \quad (3)$$

The sum of the network weights is constrained by reducing the number of effective weights to an optimized number that allows the network to fit the inputs to the training targets while also limiting the networks complexity. This makes the network's response to the presented inputs smoother and the network less prone to over fitting, hence, improving its generalization ability when confronted with new data during the application of the network later on.

The cost function weight parameter β in Eq. (3) sets the emphasis of the training algorithm towards reducing the network error term E , whereas increasing the weight parameter α sets the emphasis towards reducing the sum of the weights integrated over all network neurons. The minimization of the network errors (i.e. minimization of the cost function (Eq. (3))) was achieved using the Levenberg–Marquardt (LM) optimization algorithm as implemented in Matlab (R2017b). Combining the gradient-descent method and the Gauss–Newton minimization algorithm, we used the LM method as the iterative numerical standard approach to solve non-linear minimization problems.

A detailed description can be found in Marquardt (1963) or Butenko and Pardalos (2014). Both the search for the best network weights during the LM iteration and the search for the best number of active weights were regularized based on a Bayesian approach by optimizing the cost function weight parameters α and β . Following MacKay (1992) and Foresee and Hagan (1997) we maximize the posterior of the probability density function applying Bayes' rule:

$$P(d|\alpha, \beta, M) = \frac{P(d|\mathbf{w}, \beta, M) \cdot P(\mathbf{w}|\alpha, M)}{P(\mathbf{w}|d, \alpha, \beta, M)}. \quad (4)$$

Here, d is the available dataset with inputs and targets, M is the network model, and \mathbf{w} is the vector of neural network weights. Assuming a Gaussian distribution for the random noise in the training data and for the prior distribution of the network weights that are, in fact, initialized randomly in the algorithm, the probability terms in the numerator can be substituted through,

$$P(\mathbf{w}|\alpha, M) = \frac{1}{Z_{\mathbf{w}}(\alpha)} \exp(-\alpha E_{\mathbf{w}}) \quad (5)$$

and

$$P(d|\mathbf{w}, \beta, M) = \frac{1}{Z_d(\beta)} \exp(-\beta E), \quad (6)$$

and Eq. (4) can be written as:

$$P(d|\alpha, \beta, M) = \frac{\left[\frac{1}{Z_d(\beta)} \exp(-\beta E) \right] \left[\frac{1}{Z_{\mathbf{w}}(\alpha)} \exp(-\alpha E_{\mathbf{w}}) \right]}{\frac{1}{Z_F(\alpha, \beta)} \exp(-F(\mathbf{w}))} \\ = \frac{Z_F(\alpha, \beta)}{Z_{\mathbf{w}}(\alpha) \cdot Z_d(\beta)}, \quad (7)$$

with $Z_d(\beta) = (\pi/\beta)^{n/2}$ and $Z_{\mathbf{w}}(\alpha) = (\pi/\alpha)^{N/2}$.

After approximating Z_F in through a Taylor series, solving for the denominator in Eq. (4) we get:

$$Z_F \approx (2\pi)^{N/2} (\det(\mathbf{H}^{MP})^{-1})^{1/2} \cdot \exp(-F(\mathbf{w}^{MP})), \quad (8)$$

where MP indicates the corresponding values at the minimum point of the cost function or the maximum posterior of the probability density $P(d|\alpha, \beta, M)$, respectively. \mathbf{H} is the Hessian matrix of the cost function containing the second order partial derivatives of $F(\mathbf{w})$.

Substituting Z_F in Eq. (7) by the approximation of Eq. (8) and setting the first derivative of Eq. (7) equal to zero yields the values for the weight parameters at the minimum of the cost function:

$$\alpha^{MP} = \frac{\mu}{2E_{\mathbf{w}}(\mathbf{w}^{MP})} \quad (9)$$

And

$$\beta^{MP} = \frac{n - \mu}{2E(\mathbf{w}^{MP})} \quad (10)$$

$$\text{with } \mu = N - 2\alpha^{MP} \text{Tr}(\mathbf{H}^{MP})^{-1}. \quad (11)$$

Here, μ is the minimized effective number of parameters in the optimized network and gives the number of parameters in the network that were effectively used to minimize F . Tr indicates the trace of the inverse Hessian matrix, summed at the minimum point found in Eq. (11).

The 36 DTDNNs (9 vegetation types \times 4 target variables) used within this study were trained until the sum-squared error, the sum-squared weights, and the effective number of parameters converged at their optima. Initial values of α and β were set to 0.5, equalizing the priority of MSE minimization and the minimization of the mean squared sum of the weights at the beginning of the learning process.

For the training procedure, all DTDNN models were initialized with 40 neurons in the hidden layer. The number and values of the active parameters were set, based on the Bayesian regularized LM optimization. The initial number of hidden neurons ensures that each network is powerful enough to closely reproduce the training data and potentially over-fit while the Bayesian regularization constrains the number of active parameters to acquire the optimal function generalization ability for each model.

2.4. Model classification of LULC

The vegetation land cover in our model domain was classified and assigned using Landsat series of satellites. This dataset constitutes the longest existing satellite record of terrestrial vegetation, starting in 1972, and maturing with the Landsat MSS and TM instruments since 1984. Landsat's spatial resolution of 30 m and its extent of 185×185 km per scene have proven utility for monitoring vegetation change at regional scales. We have obtained and processed Landsat observations across the state of Oregon (24 path rows), a total of 12 500 scenes to map changes in land cover. Landsat observations were combined into best available pixel mosaics representing the period between April and July for each year from 1984 to 2012. Land cover types were separated using an unsupervised K-means clustering approach. Next, land cover classes were assigned based on a forest type map described in Ruefenacht et al. (2008). The assumption was that the distribution of vegetation types changes only gradually from one year to the next in a 100 km^2 area. It was also assumed that vegetation types were assigned using the closest matching distribution of land cover types in a locally moving window. To distinguish non-forage grass from other grasses we used the 30 m resolution Cropland Data Layer (CDL 2015) provided by the National Agricultural Statistics Service of the United State Department of Agriculture (<https://nassgeodata.gmu.edu/CropScape/>).

In order to assign the available flux datasets from an old (US-Me2) and a young (US-Me6) stand of *Pinus ponderosa*, we used the Forest Age Maps at 1-km Resolution for Canada and the U.S.A. provided by the North American Carbon Program (NACP) (Pan et al., 2011).

We aggregated the stand age data to our 4 km spatial resolution grids for the assignment of the flux values during the DTDNN model runs. Thus, to separate the two age classes resolved by our flux tower training data and consequently our DTDNN model ensemble, the pine group was divided into <40 years and ≥ 40 years within the Oregon domain. During the runs, the respective model developed with the data from the sites US-Me2 (stand age ≥ 40 years) and US-Me6 (stand age <40 years) was specifically applied to the pine group of each individual grid cell during the model

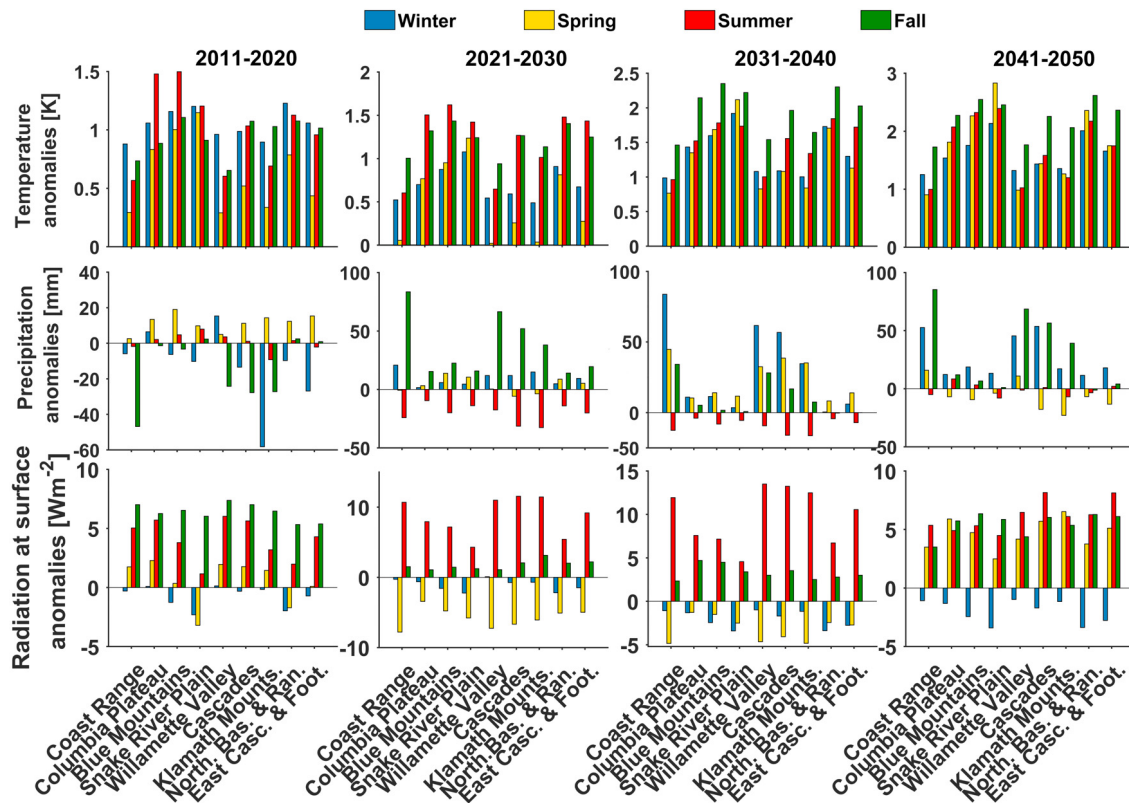


Fig. 3. Seasonal decadal and ecoregion-specific anomalies of downscaled climate elements used as model input. Anomalies were calculated based on the 30-year normal of 1981–2010.

runs. This accounted for age-dependent physiological responses by the available flux towers in our domain.

We then calculated the fractions of the 9 land cover types in each $1/24^\circ \times 1/24^\circ$ grid cell. Using percent land cover values accounts for sub-grid effects of vegetation composition. By representing the land cover with all possible compositions within a limited number of main vegetation types we were able to extrapolate the modeled fluxes over the entire domain using the 36 specific DTDNN models. This fractional land cover approach used to generalize a land surface parameterization with limited spatial information (or limited site specific ANN flux models as in our case) is also successfully applied in the land model component (CLM) of the Community Earth System Model (CESM). This method comprehensively addresses the mixed land cover with the limited number of vegetation type-specific models or parameters available (Oleson, Lawrence, et al., 2013).

3. Results and discussion

3.1. Projected regional climate inputs

The region-specific anomalies for 3 important climate variables (T_{air} , R_{SW} and P) used in our models were calculated for each season based on the 30 year reference interval from 1981–2010. The results show that the development of the climate variables varies significantly among the ecoregions (Fig. 3). While the air temperature in the first decade from 2011–2020 shows the highest anomalies in winter for most regions with regional average increases from 0.8 K (Coast Range) to 1.2 K (Northern Basin and Range high desert region), the later periods from 2031–2050 show the most significant changes during the transitional seasons between the hot and dry summers and wet winters in Oregon.

The highest anomalies in air temperature occur the in eastern ecoregions of the state (e.g. Columbia Plateau, Northern Basin

and Range, or the Eastern Cascades) during fall, with the highest anomaly being 2.8 K in the Snake River Plain region (Fig. 1) during spring in the decade 2041–2050 (Fig. 3).

Throughout the current decade, precipitation anomalies show an overall decrease. These conditions are followed by an increase in fall and winter precipitation compared to the reference period for all ecoregions. This increase is in contrast to summer precipitation which is predicted to decrease by 30 to 40 mm per summer, on average, from 2021 to 2040 but re-approaches the normal from 2041–2050 (Fig. 3, middle row). Shortwave radiation reaching the surface changes by up to 10 Wm^{-2} during the summer months.

Obvious negative anomalies occur in spring for the decade ahead (2021–2030) during which climate projections indicate a maximum decrease of incoming shortwave radiation at the surface for the Coast Range region of 8 Wm^{-2} , most likely due to increased cloud formation.

Detailed discussions of the processes that cause the changing climate can be found in the corresponding literature addressing the CMIP 5 model results (e.g. Taylor et al., 2012) or the respective downscaling methods (Abatzoglou & Brown, 2012). The regionally varying changes of climate drivers over the next three decades suggests that, in combination with the distinct vegetation cover in those areas, and, correspondingly different responses to meteorological conditions, the total changes of the statewide NEP and energy fluxes will not increase or decrease linearly over longer time periods but instead show strong variations in responses of the biosphere in different regions of the state.

Of particular interest are the changes in climate conditions for the regions that could be most affected by anticipated LULC change. The Willamette Valley and Columbia Plateau are regions that are most likely to be converted to bioenergy hybrid poplar plantations due to their high amount of seed grass crops and other non-forage grass. In addition, these two regions already have the irrigation infrastructure needed for poplar plantations.

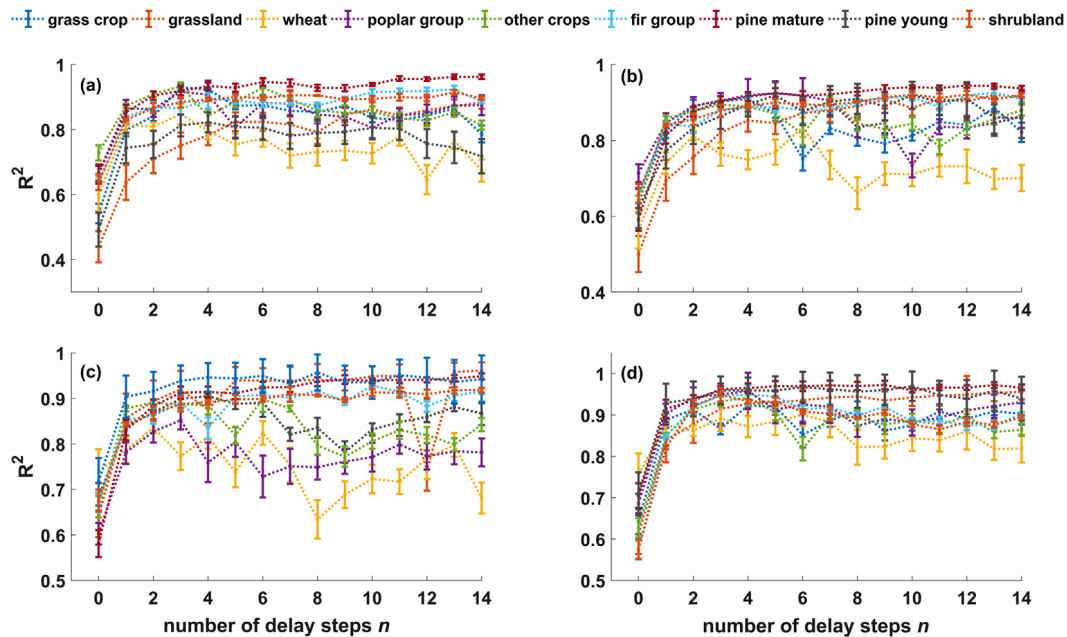


Fig. 4. Coefficients of determination R^2 for the test data for all time delays tested and all land cover types of the DTDNN ensemble. R^2 is shown for NEE (a), LE (b), H (c), and R_{net} (d). The R^2 values at $n = 0$ (abscissa) correspond to coefficients as obtained using a network with non-delayed inputs but otherwise identical network topography. The error bars denote the variation among all models tested for a land cover type and extend of temporal delay.

Table 2

Coefficients of determination for each LULC class averaged over all target variables NEE , LE , H , and R_{net} .

LULC/ network group	$R^2(n = 0)$ no time- delayed input	$R^2(n > 0)$ time-delayed input	Performance increase (%)
Grass crop	0.57	0.94	64.9
Grassland	0.54	0.96	77.8
Wheat	0.54	0.84	55.6
Poplar group	0.55	0.86	56.4
Other crops	0.52	0.83	59.6
Fir group	0.62	0.96	54.8
Pine (mature)	0.59	0.92	55.9
Pine (young)	0.53	0.95	79.3
Shrubland	0.56	0.95	69.6
Average	0.56	0.91	63.8

3.2. DTDN model evaluation

Using the test data, the model-data comparisons also show that the performance of the network models reach maxima for R^2 at different delays (Fig. 4). The measurement-model inter-comparisons in Fig. 4 show the DTDNN test results for all 9 LULC classes in our model ensemble for which measurement data was available for model training and evaluation.

The coefficients of determination improved significantly in all cases when delayed input vectors were used. Compared to the common network setup with only temporally corresponding inputs ($n = 0$), R^2 could be increased by 64% on average using the best delay value for all fluxes and all LULC types. The values shown in Table 2 are from the measurement-data comparisons of the test dataset. We compared the coefficients reached with the networks with non-delayed inputs to the corresponding values that were achieved by using the network with the lowest error and highest R^2 for the test data using delayed time series input vectors.

The model performance, measured by R^2 , does reach maximum extents for each LULC network model despite the addition of information from previous input variables that can still affect the output. In fact, as shown in Fig. 4, the model performance decreases, in some cases, when longer time series vectors beyond the optimum delay are used as inputs. This effect observed with our training data series shows that adding more input values from increasingly earlier time periods no longer benefits the accuracy of

the target values as a saturation of information that is useful for to map the input on the target is reached. Instead, adding even more input data starts to decrease the correlation between the measured and modeled target values (Fig. 4). This effect, often referred to as the ‘curse of dimensionality’ and mathematically described in the corresponding literature (e.g. Bengio & Bengio, 2000; Bishop, 2006), is caused by the increasing complexity of the error function to be minimized which makes finding the global error minimum more difficult due to the increasing number of variables considered.

At 3-hourly resolution, the interval in which the modeled fluxes and radiation are mathematically dependent on backward inputs can only be determined with a corresponding temporal resolution. For the fluxes and net radiation the optimized delays with the highest R^2 values do not exceed $12\Delta t$ (Fig. 4) which corresponds to a delayed effect of the climate input on the fluxes of 36 h. For the final prediction model runs the winning networks with the highest R^2 where chosen for each specific LULC. While there are climate events such as droughts that will affect ecosystem NEE , H , and LE for more than several days, the effects covered by the 36 h are solely primary effects of the meteorology on the fluxes. Effects of droughts with long-term effects on LE and NEE , however, are secondary and related to diminishing subsurface water supplies and stress symptoms (Hoover & Rogers, 2016; Mekonnen, Grant, & Schwalm, 2017). Those secondary effects are considered in

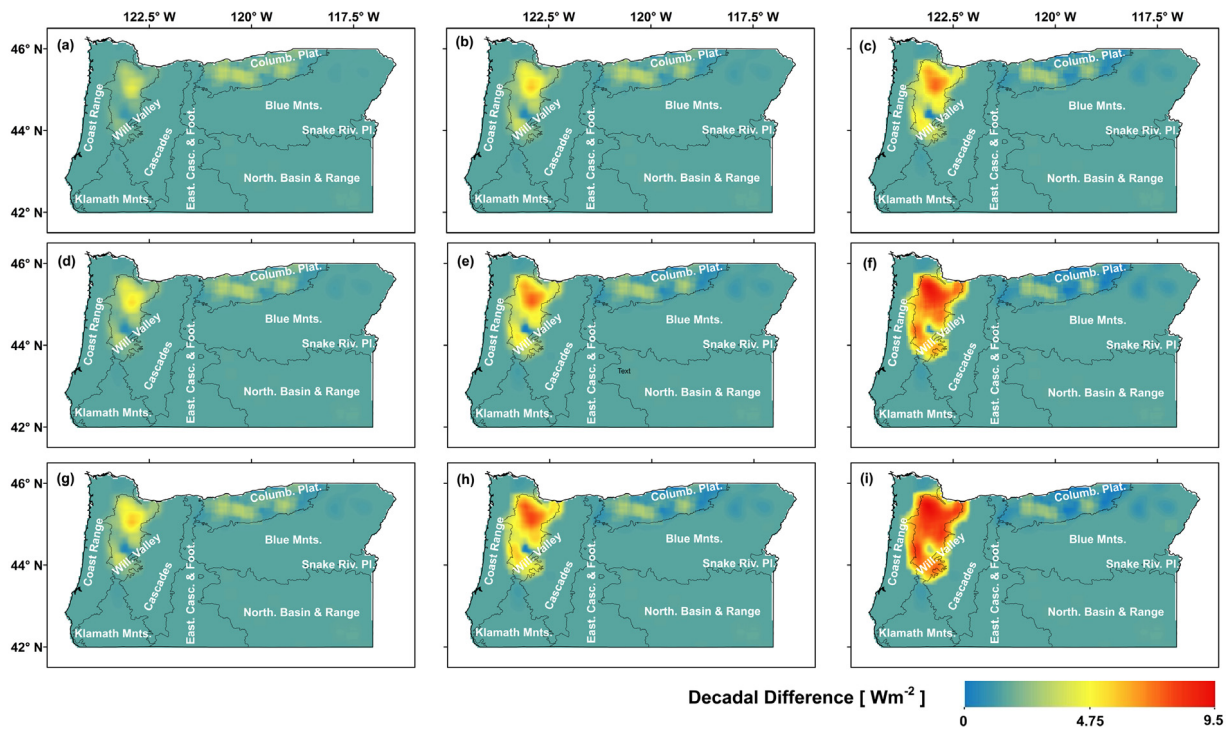


Fig. 5. Spatial Differences in average R_{net} (scenarios—BAU) for the 3 decades 2021–2030 (top row), 2031–2040 (middle row), and 2041–2050 (bottom row) for LULC scenario 1 (a, d, g), scenario 2 (b, e, h), and scenario 3 (c, f, i).

our approach only through the application of multi-year learning datasets that incorporate such conditions.

Four of our nine vegetation cover types are managed and irrigated crops. Irrigation can be especially challenging when modeling energy exchange because of the altered Bowen ratio ($B=H/LE$) associated with the change in partitioning of energy fluxes following irrigation events. Given the high correlations achieved by the DTDNN models, the LE and H models reliably captured the functional relationship between the physical cause (irrigation) and the delayed effect (altered Bowen ratio) (Fig. 4).

3.3. Net radiation and Bowen ratio

The effects of LULC on net radiation and heat fluxes were modeled using the DTDNN models and projected climate data. Land conversion from annual non-forage grass to hybrid poplar through year 2050 was separated into 3 scenarios with different annual conversion rates. We then calculated the difference between results for the BAU scenario and the results of the 3 conversion scenarios averaged over the next 3 decades from 2021 to 2030, 2031 to 2040, and 2041 to 2050. With the effect of the climate input superimposed on both the BAU and the LULC change scenario runs, the differences between the two show the distinct effect of the LULC conversion.

Gradual conversion rates of 2% (Fig. 5, left Column), 5% (Fig. 5, middle column), and 10% (Fig. 5, right column) per year from non-forage grass crops to bioenergy hybrid poplar, primarily affect R_{net} at the surface. As the dense, higher albedo (0.21) grass fields are replaced, more energy is absorbed by the poplar foliage and exposed surface, gradually increasing R_{net} (Fig. 5). Consequently, net radiation increases noticeably in the Willamette Valley when the non-forage grass crops are replaced by deciduous hybrid poplar trees. Smaller changes occur in the Columbia Basin ecoregion where the majority of grass crops are grown as hay for livestock feed which leads to smaller changes in LULC.

With all of the non-forage grass fields converted, net radiation increases by 4.1 Wm^{-2} on average ($\sigma = 2.01 \text{ Wm}^{-2}$) in the

Willamette Valley where the spatial extent of non-forage grass crops is the largest in the state. Compared to BAU, the Columbia Basin exhibits changes in R_{net} averaging 0.3 Wm^{-2} ($\sigma = 0.09 \text{ Wm}^{-2}$) during 2041 to 2050 (Fig. 5i). Assuming the lowest LULC conversion rate of 2% per year, the decadal offset values in the Willamette Valley ecoregion are 0.11 Wm^{-2} ($\sigma = 0.09 \text{ Wm}^{-2}$), 0.25 Wm^{-2} ($\sigma = 0.31 \text{ Wm}^{-2}$), and 0.36 Wm^{-2} ($\sigma = 0.42 \text{ Wm}^{-2}$), respectively (Fig. 5a, d, g). The results show the significant effect the conversion of land cover has on the surface radiation budget in the Willamette Valley ecoregion.

To examine the effect of LULC change on energy partitioning in the region we calculated the Bowen ratio. The significant impact of LULC on R_{net} in the Willamette Valley is reflected by the energy partitioning expressed by the Bowen ratio of the sensible heat flux and latent heat fluxes as given in Fig. 6. The modeled average increase of R_{net} leads to an overall increase of the heat fluxes due to the surplus radiation energy warming up the surface and canopy.

The figures showing the corresponding results for H and LE can be found in Appendix B. Due to the intensive irrigation practices on hybrid poplar plantations (Vasquez & Milota, 2017) evaporation and thus LE are expected to increase after LULC conversion, which is confirmed by the model results.

Irrigation provides the moisture to increase LE and correspondingly mitigate the increase of H . Thus, the average Bowen ratio decreases during most decades and rates of conversion. There are a few local exceptions where the Bowen ratio increases slightly by 0.15 (Fig. 6) in small areas in the southern and central Willamette Valley ecoregion (Fig. 6f, h, and i). This can be attributed to areas where irradiation to the surface and precipitation (Fig. 3) lead to inherently low Bowen ratios. After full conversion of the crop land to poplar plantations, the average decrease in Bowen ratio within the Willamette Valley averages -0.18 ($\sigma = 0.08$).

Given 50% of the LULC conversion in the state, the average decrease of the Bowen ratio is predicted to be -0.10 ($\sigma = 0.05$) in the Willamette Valley and -0.01 ($\sigma = 0.02$) for the Columbia Basin, respectively.

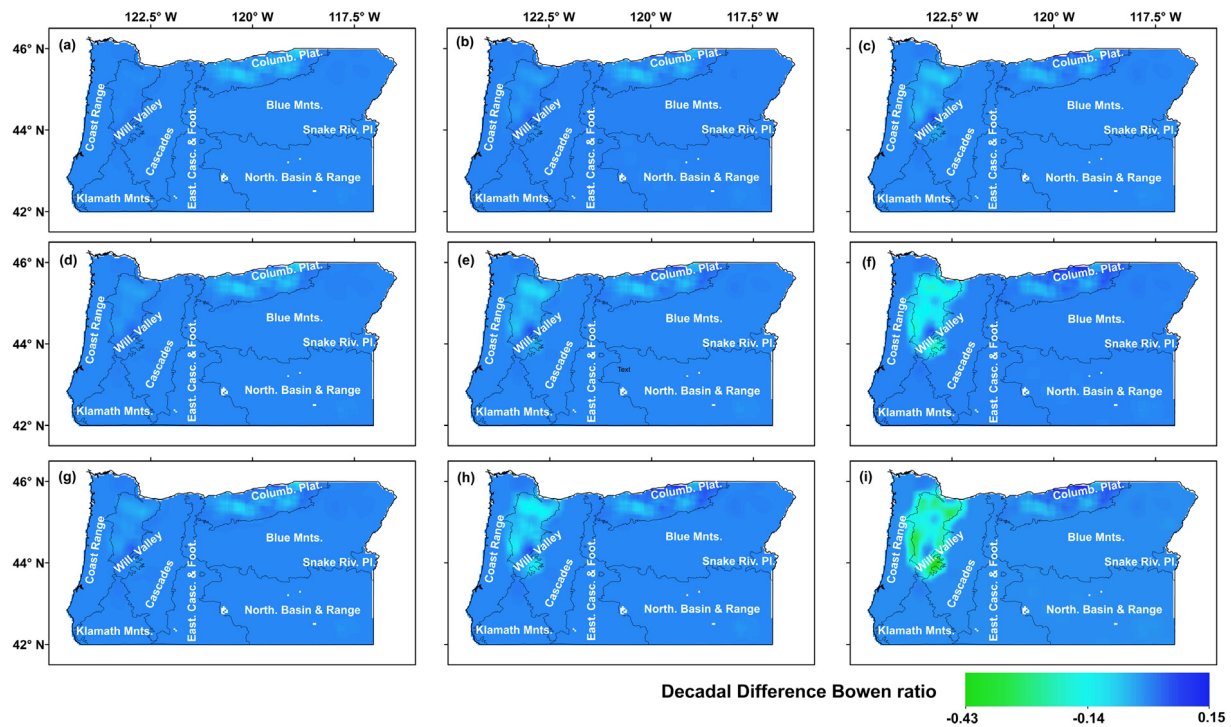


Fig. 6. Spatial Differences in average Bowen ratio (H/LE) (scenarios—BAU) for the 3 decades 2021–2030 (top row), 2031–2040 (middle row), and 2041–2050 (bottom row) for LULC scenario 1 (a, d, g), scenario 2 (b, e, h), and scenario 3 (c, f, i). A negative (e.g. green) value means the Bowen ratio decreased through time. (For interpretation of the references to color in this figure legend, the reader is referred to the web version of this article.)

Table 3

Average annual NEP and standard deviations for the Level III ecoregions in Oregon. The standard deviations indicate the inter-annual variability in NEP.

	Posterior NEP (TgC year ⁻¹)	σ (TgC year ⁻¹)	NEP DTNN (TgC year ⁻¹)	σ (TgC year ⁻¹)
Coast Range	9.23	1.26	8.02	1.53
Willamette Valley	2.48	1.48	2.81	1.58
Cascades	6.45	1.99	4.43	0.41
Eastern Cascades Slopes and Foothills	2.81	1.00	2.44	0.22
Columbia Plateau	0.81	0.31	1.70	0.32
Blue Mountains	2.55	1.36	3.34	0.13
Snake River Plain	0.19	0.13	0.31	0.21
Klamath Mountains	4.45	1.04	3.82	0.70
Northern Basin and Range	0.72	0.29	0.48	0.11
State total	29.70	8.86	27.35	5.22

As stated in Section 3.2, based on the model-data comparison using the final DTNN models, the effect of irrigation on the heat fluxes is inherent in the EC data used for the regularization and learning process of the network models. The results for LE , H , and R_{net} were used as additional model input variables for the DTNN models developed to calculate NEE and derive NEP (Fig. 2) due to their strong relationship with turbulent CO_2 exchange between the vegetation and the atmosphere.

3.4. Model validation and current net ecosystem production

We compared our NEP results with a study covering an overlapping period (2012–2014) within Oregon using a 4DVAR data assimilation process (Schmidt et al., 2016a). In that study, high precision CO_2 mixing ratio observations from five towers in Oregon were used in combination with the WRF-STILT transport model to optimize prior NEE values that were calculated with the community land model (CLM4.5) using a Bayesian inversion approach. The model domain was identical to the domain in this study with a $1/24^\circ \times 1/24^\circ$ spatial resolution. The inverse modeling results of the study showed that, without being constrained by the CO_2 observations, the process-based bottom-up land model CLM4.5 underestimated Oregon's statewide annual NEP by 32% on average

over a 3-year study period from 2012 to 2014. We compared the final results after the Bayesian data assimilation process with the results from our DTNN approach. Table 3 shows the comparison of annual NEP for each ecoregion in Oregon over the 3 year overlapping period.

Considering the fundamentally different approaches used (i.e. flux site estimates spatio-temporally interpolated with artificial neural networks versus a Bayesian inversion based on atmospheric CO_2 mixing ratios in combination with tower footprint analyses), state totals for NEP and averages over the Level III ecoregions are in very close agreement (Table 3). Statewide NEP from the DTNN results was 7.9% lower for the 3-year period compared to results from the atmospheric inversion procedure of Schmidt et al. (2016). It is important to mention that the measured fluxes from the inversion approach were also used for prior flux uncertainty estimates. Thus, while the constraining effect of the fluxes is much stronger on the DTNN model, the Bayesian atmospheric inversion study was also influenced by EC datasets as used in this study.

Based on the agreement between current and recent annual NEP values, we are confident that the DTNN models are capable of modeling reasonable fluxes based on future climate projections with high spatiotemporal resolution. After establishing the DTNN model ensemble was able to match observations under current

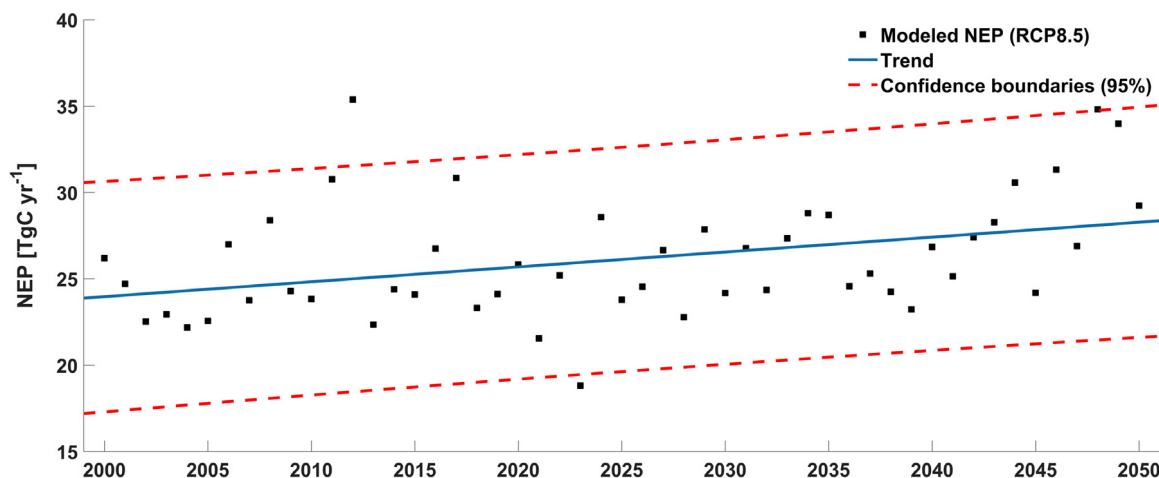


Fig. 7. Linear trend for the NEP values from 2000 through 2050 under future climate predictions assuming a business as usual (BAU) scenario with no significant changes in LULC.

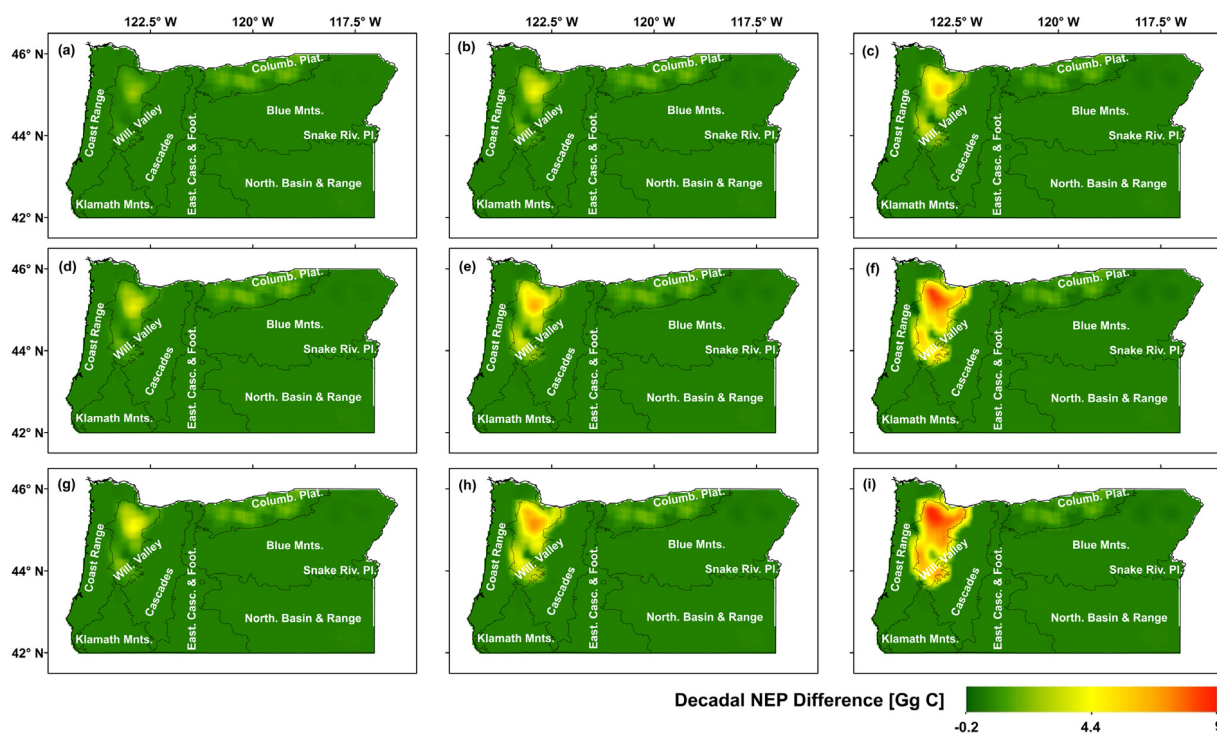


Fig. 8. Spatial Differences in average NEP (scenarios—BAU) for the 3 decades 2021–2030 (top row), 2031–2040 (middle row), and 2041–2050 (bottom row) for LULC scenario 1 (a, d, g), scenario 2 (b, e, h), and scenario 3 (c, f, i). A larger positive value (yellow to red) means NEP increased through time. (For interpretation of the references to color in this figure legend, the reader is referred to the web version of this article.)

conditions (Fig. 4 and Table 3), we simulated quantitative effects of future LULC change scenarios as defined by the state's goal to reduce greenhouse gas emissions and effects of future climate scenarios on the carbon budget in Oregon.

3.5. Future net ecosystem production

To distinguish between the effects of future climate and the LULC changes, we first calculated statewide NEP given a BAU scenario. Without any prescribed changes to LULC, predicted annual NEP increases 9% between 2016 and 2050 using the model ensemble driven by the RCP8.5 climate projection. The average decadal increase in NEP was 0.87 TgC until 2050, approximated by a linear trend with a 95% confidence interval (Fig. 7).

Annual fluctuations of NEP are high throughout the study period from 2000 to 2050 due to the impact of varying climate over the 51 year period analyzed (Fig. 7). Similar strong inter-annual fluctuations of NEP were also found in other studies investigating statewide annual NEP of the terrestrial biosphere in Oregon in recent years (e.g. Turner et al., 2011, 2007).

In Fig. 8 the spatial patterns of the NEP changes and decadal averages are presented for the 3 conversion scenarios. The largest increases in NEP are predicted for the central and southern Willamette Valley. Here, maximum changes of 9 Gg C occur per decade within a 4×4 km grid in which 100% of land is converted (Fig. 8f and i).

The ecoregion-specific results show spatially distinct NEP estimates given different LULC conversion scenarios (Fig. 9). Changes in NEP are similar across ecoregions in the first decade following

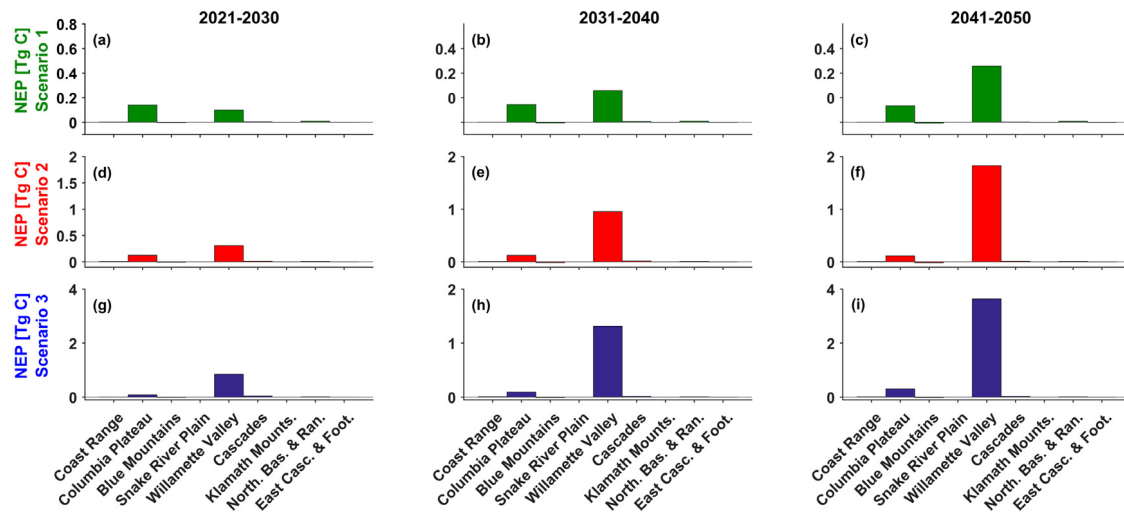


Fig. 9. Decadal region-specific changes of annual average NEP (Scenarios—BAU). Significant NEP changes due to LULC changes are found in the Willamette Valley and the Columbia Basin ecoregions.

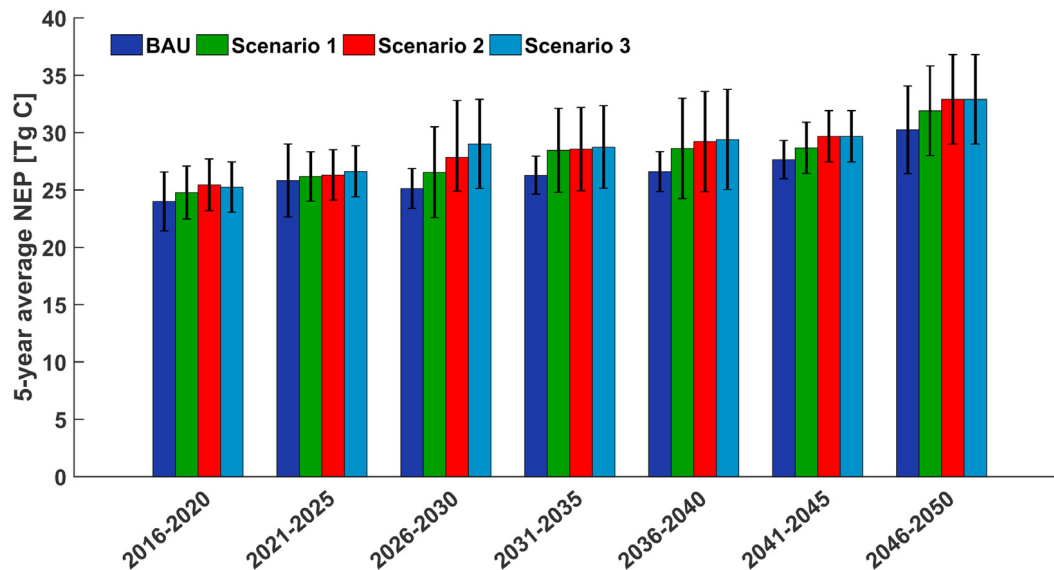


Fig. 10. 5-year averages of the absolute statewide NEP from 2015–2050 for the BAU scenario and the anticipated LULC change scenarios with annual replacement rates of 2% (scenario 1), 5% (scenario 2), and 10% (scenario 3). The error bars denote the 1σ inter-annual fluctuations of the binned values.

conversion (Fig. 9a, d, g). Over time, and increasing with conversion rate, the effects of LULC are greatest in the Willamette Valley. The effects in other ecoregions are negligible due to the small amount of grass crops suitable for conversion to bioenergy poplar plantations (Fig. 9).

With 100% of the grass converted to hybrid poplar, the sum of NEP changes in the Willamette Valley and the Columbia Basin averages 3.94 TgC over the ten-year period from 2041 to 2050 (Fig. 9). The total statewide NEP results in Fig. 10 show the overall increase of biosphere CO_2 -related carbon uptake after conversion over 50 years as well as within 5 year averaging blocks. The shorter averaging interval shows the fluctuations of total statewide NEP over time with and without altered vegetation surface. While the long-term NEP increases, there are periods with decreasing NEP, compared to the previous 5-years, indicating the meaningful effect of climate variables that govern photosynthesis and respiration processes.

Using the linear trend approximation (Fig. 7) the annual NEP rises by 3.48 TgC on average from 2016 to 2050 due to climate change and increased atmospheric CO_2 (RCP8.5) and current land

use. If 50% of the grass crops in Oregon are replaced by hybrid poplar, another 1.09 TgC will be added to the annual average NEP. If all non-forage grass crops are converted, annual average NEP increases by 3.94 TgC with contributions varying significantly from the distinct ecoregions (Figs. 9 and 10).

The NEP changes start equalizing in the ten years between 2041 and 2050 when all areas with non-forage grass crops in the state are converted to hybrid poplar plantations given the LULC change rates prescribed in scenario 2 and 3. The 5-year averages of total statewide annual NEP under the BAU scenario change from 23.99 TgC (± 2.57 TgC) in 2016–2020 to 30.21 TgC (± 3.82 TgC) in the years 2046–2050 (Fig. 10). The total annual NEP with the grass converted to poplar averages 32.9 TgC (± 3.88 TgC) in 2046–2050. Thus, state-level NEP is predicted to increase 26% by 2050 due to a changing climate assuming the RCP8.5 and current land use, while the conversion of all non-forage grass to poplar is predicted to increase annual NEP by 9%.

We determined the theoretical maximum amount of torrefied biomass that could be produced for bioenergy production by the energy facility if the land-use change scenario of non-forage grass

to poplar was implemented. The power facility torrefies the wood (pyrolysis at high temperatures to reduce moisture) prior to combustion. Conversion of all the non-forage grass to poplar would provide about 1.1 TgC yr^{-1} torrefied biomass or 37% of the required biomass at base load. However, this calculation does not account for the emissions associated with transportation of wood from the plantations to the facility, torrefaction, and the bioenergy burning itself, which is an immediate emission of carbon dioxide to the atmosphere. Further work using life cycle assessment is necessary to compute the carbon consequences of this land use change to poplar plantations. In addition, the competition for land and resistance to change the grass cash crop to bioenergy would likely reduce the actual amount of land that could be converted to bioenergy poplar plantations.

4. Summary and conclusion

We modeled the effect of land cover change on NEP using different conversion rates from non-forage grass crops to hybrid poplar plantations in Oregon. The analysis was driven by realistic numbers defined by the state mandate to reduce CO_2 emissions by the year 2020. Crop conversion was based on the state's plan to cease use of coal in favor of bioenergy at its last remaining coal power plant.

We developed DTDNN models to simulate the effect of LULC change on heat fluxes, net radiation, and finally *NEP* using data from 9 EC flux sites. The DTDNN networks enable the network to also incorporate previous states of the input space driving the model output. The results show that the DTDNN models reduce the error during data-model comparison significantly and increase the coefficients of determination for H , LE , R_{net} , and *NEP* by 64%, on average, showing the potential of this machine learning approach for ecosystem modeling.

Intensive irrigation of poplar plantations is observed across the state. As a result, the analysis predicted a long-term decrease in statewide Bowen ratio with LULCC from grass to poplar because of the higher evapotranspiration, which is consistent with other regional analyses. In the Northern Great Basin ecoregion irrigation over large areas and long periods significantly decreased the ratio of sensible to latent heat. It also led to reductions of minimum, maximum, and average long-term air temperature near the surface with strong gradients from irrigated to non-irrigated areas (Mahmood, Hubbard, & Carlson, 2004).

Annual values of *NEP* vary significantly. However, using a linear trend approximation, the annual *NEP* rises by 3.48 TgC , on average, between 2010 and 2050 assuming current LULC distribution in Oregon and climate developments associated with the RCP8.5.

The LULC change will add another 1.09 TgC to the annual average *NEP* once 50% of the grass crops are replaced by hybrid poplar and another 3.94 TgC assuming a complete conversion. Contributions vary significantly between the distinct ecoregions (Figs. 9 and 10). Nevertheless, the deviations from the decadal averages to the 5-year averages are reasonably small. While the changing climate itself increases *NEP* by 0.89 TgC per decade, the partial conversion of the vegetation adds an average of roughly 4 TgC , totaling $32.9 (\pm 3.88) \text{ TgC}$ per year for the statewide *NEP* by 2050. Hence, state-level annual *NEP* is predicted to increase 26% by 2050 due to changing climate, increasing atmospheric CO_2 , and current land use, and land-use change of all non-forage grass to poplar is predicted to increase annual *NEP* by 9%.

Our results also show suitability of the DTDNN models that can capitalize on the temporal data richness if measured EC and meteorological time series are available to train the model. Here, we used sub-daily modeling and measurement steps to simulate the direct ecosystem responses and assess the effect of potential future land use changes under future climate projections.

Analyzing the ecosystem responses on different temporal scales will provide information on how long drought effects influence ecosystem productivity in succeeding years. Using available flux and climate data to address large scale responses using this DTDNN machine learning approach is a goal for future studies.

Acknowledgments

This research was supported by the U.S. Department of Energy (Grant number DE-SC0012194) and the Agriculture and Food Research Initiative of the USDA National Institute of Food and Agriculture (Grant numbers 2014-67003-22065 and 2014-35100-22066). Funding for *AmeriFlux* data resources was provided by the U.S. Department of Energy's Office of Science. The authors thank David Rupp for the downscaling of the climate input data. The daily METDATA observation dataset and the spatially downscaled MACA data from the CMIP5 project are provided by the University of Idaho and made accessible through the webpage <http://maca.northwestknowledge.net>. PRISM climate data is provided by the PRISM climate group at Oregon State University and made accessible through the webpage <http://prism.oregonstate.edu>.

Appendix A. Climate input data

The source of the climate variables used to create the down-scaled high resolution ($1/24^\circ$, 3-hourly) climate dataset for the network model runs are simulations using the global climate model (GCM) MIROC5 as part of the Coupled Model Intercomparison Project Phase 5 (CMIP5; Taylor et al., 2012). The MIROC5 simulations were statistically downscaled and bias corrected using Multivariate Adaptive Constructed Analogs (MACA; Abatzoglou & Brown, 2012). The MACA algorithm samples from a dataset of gridded observations (training data) using spatial pattern matching for the variable from the Global Climate Model (GCM) and the training data. The daily climate data of the METDATA dataset (Abatzoglou, 2013) with a horizontal resolution of $1/24^\circ \times 1/24^\circ$ was used as training data for the MACA algorithm.

For the disaggregation of the downscaled daily data to a 3-hourly resolution, we made use of the 3-hourly data from the original CMIP5 datasets. The method consists of rescaling the 3-hourly GCM time series to be consistent with aggregated daily values, or maximum and minimum daily values, from MACA. This entails first converting the variables in the 3-hourly global climate model datasets to dimensionless quantities by some standardization method (the particular method will depend on the variable). Second, the downscaled daily data is disaggregated to 3-hourly by multiplying the daily data by the standardized quantities. To apply the second step, each fine-grained cell in the downscaled dataset set must be mapped to its associated coarse-grained cell in the GCM dataset. The strength of this method is that it maintains the covariance structure of, and therefore the physical consistency between, all the variables. First, each variable is standardized in the GCM dataset. To transform the temperature T , we use the following standardization:

$$T_i^* = \frac{T_i - (T_{\max} + T_{\min})/2}{T_{\max} - T_{\min}} \quad \text{for } T_{\max} \neq T_{\min}, \quad (\text{A.1})$$

where the asterisk indicates the standardized quantity, i is the index of the 3-hour time step within a 24 h day (1, 2, ..., 8), and T_{\max} and T_{\min} are the daily maximum and the daily minimum temperature values, respectively.

If $T_{\max} = T_{\min}$ we use:

$$T_i^* = \frac{1}{2} \sin \left[\frac{\pi}{12} (t_{\text{local}} - 9) \right], \quad (\text{A.2})$$

where T_{local} is the local time (0 to 24 h). Eq. (A.2) sets the minimum and maximum temperatures to decrease at 3:00 and 15:00 h, local time, respectively.

For the precipitation P the total within a 3-hourly period is divided by the total precipitation on that day:

$$P_i^* = \frac{P_i}{\sum_{i=1}^8 P_i} \quad \text{for} \quad \sum_{i=1}^8 P_i > 0, \quad (\text{A.3})$$

else

$$P_i^* = \frac{1}{8}. \quad (\text{A.4})$$

Relative humidity is standardized correspondingly to the algorithm used for the temperature (Eqs. (A.1) and (A.2)). Downward shortwave radiation SW used in CLM is standardized by the mean of SW over the day:

$$SW_i^* = \frac{SW_i}{\frac{1}{8} \sum_{i=1}^8 SW_i} \quad \text{for} \quad \sum_{i=1}^8 SW_i > 0, \quad (\text{A.5})$$

else

$$SW_i^* = 1. \quad (\text{A.6})$$

In case of wind, anomalies of the velocity vector components (index c) are generated as differences from the daily mean of that component:

$$\tilde{U}_{ci} = U_{ci} - \bar{U}_c, \quad (\text{A.7})$$

with the overbar indicating the daily average of the 3-hourly values.

To disaggregate the daily data to 3-hourly, each fine-grained cell in the downscaled dataset must first be mapped to its parent coarse-grained cell in the GCM. This mapping assigns each cell in the downscaled grid the location of its GCM parent cell. Once the parent location is known, the disaggregation consists of inverting the standardization procedure, with the difference that the standardization parameters are now taken from the downscaled daily data instead of the GCM data. In the case of temperature, the

standardization parameters are t_{\max} and t_{\min} :

$$t_i = t_{\max} \left(T_i^* + \frac{1}{2} \right) - t_{\min} \left(T_i^* - \frac{1}{2} \right), \quad (\text{A.8})$$

where the lower-case variable name denotes the downscaled value.

For precipitation, the parameter is the total precipitation p_{tot} of the respective day:

$$p_i = P_i^* \cdot p_{\text{tot}}. \quad (\text{A.9})$$

Disaggregating the relative humidity values is conducted using the same approach as applied to the temperature. For shortwave radiation, the standardized time series is multiplied by the mean shortwave radiation on a given day:

$$sw_i = SW_i^* \cdot \bar{sw}. \quad (\text{A.10})$$

For the wind vectors the 3-hourly anomalies from the GCM were added to the daily downscaled mean wind vector components \bar{u}_c :

$$u_{ci} = \bar{u}_c + \tilde{U}_{ci}. \quad (\text{A.11})$$

This preserves the downscaled daily wind speed values that were calculated using the mean the wind components \bar{u}_c .

Appendix B. Changes of average sensible and latent heat fluxes

For the sake of completeness the decadal differences for H and LE between the LULC change scenarios and unchanged LULC (BAU) can be found in Figs. B.1 and B.2, respectively. The results correspond to the Bowen ratio discussed in Section 3.3.

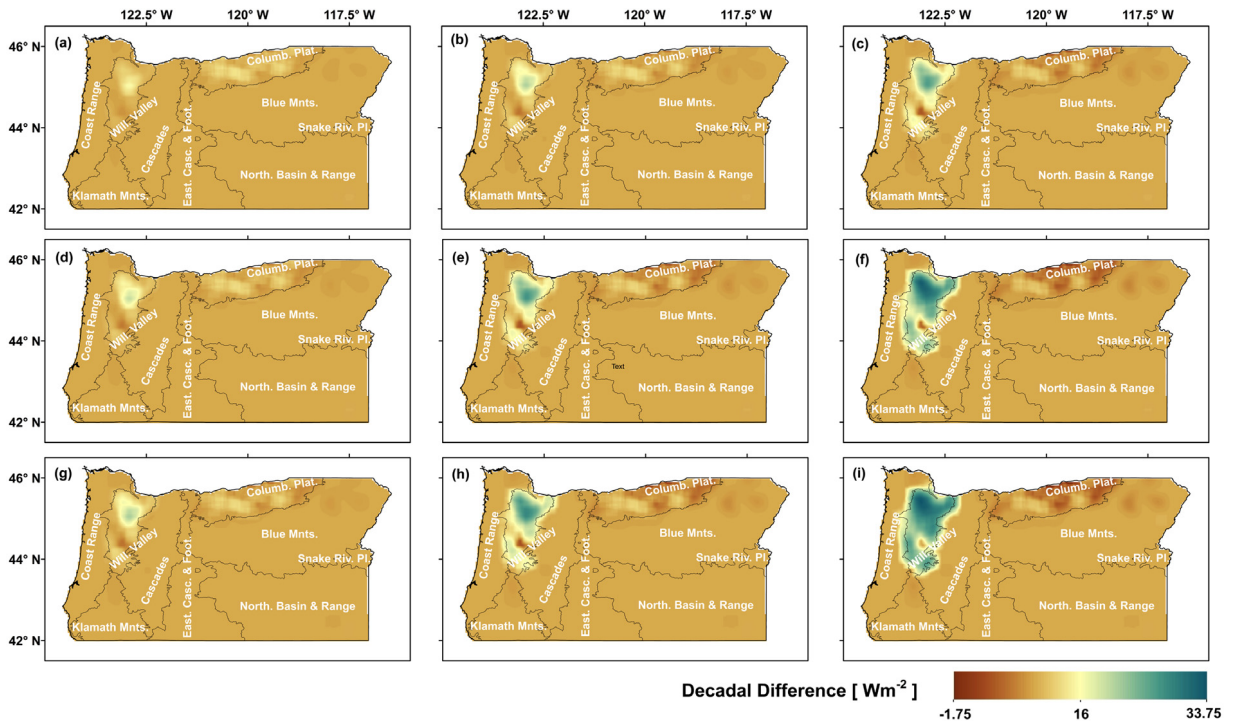


Fig. B.1. Spatial Differences in average sensible heat flux H (scenario—BAU) for the three decades 2021–2030 (top row), 2031–2040 (middle row), and 2041–2050 (bottom row) for LULC scenario 1 (a, d, g), scenario 2 (b, e, h), and scenario 3 (c, f, i).

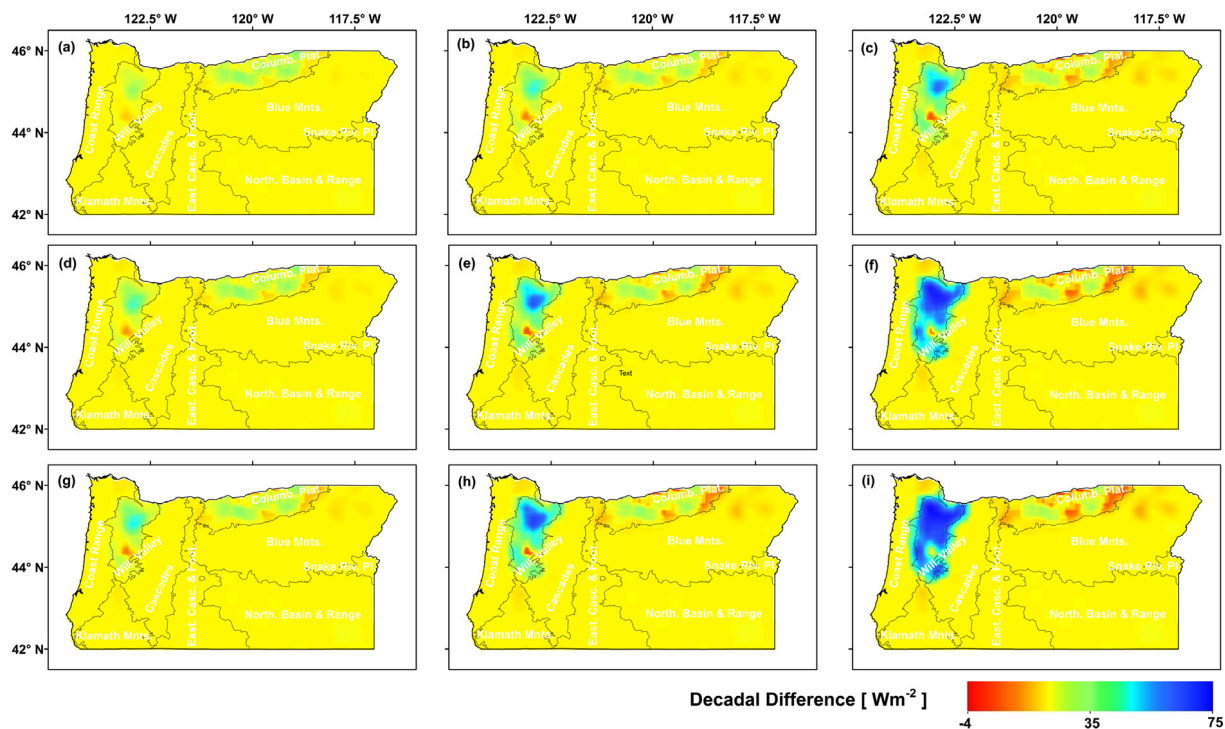


Fig. B.2. Same as Fig. B.1 but for latent heat flux LE .

References

- Abatzoglou, J. T. (2013). Development of gridded surface meteorological data for ecological applications and modelling. *International Journal of Climatology*, 33, 121–131.
- Abatzoglou, J. T., & Brown, T. J. (2012). A comparison of statistical downscaling methods suited for wildfire applications. *International Journal of Climatology*, 32, 772–780.
- Baldocchi, D. D. (2003). Assessing the eddy covariance technique for evaluating carbon dioxide exchange rates of ecosystems: Past, present and future. *Global Change Biological*, 9, 479–492.
- Baldocchi, D. D., Falge, E., Gu, L., Olson, R., Hollinger, D., Running, S., et al. (2001). FLUXNET: A new tool to study the temporal and spatial variability of ecosystem-scale carbon dioxide, water vapor, and energy flux densities. *Bulletin of the American Meteorological Society*, 82, 2415–2434.
- Bengio, S., & Bengio, Y. (2000). Taking on the curse of dimensionality in joint distributions using neural networks. *IEEE Transactions on Neural Networks, special issue on Data Mining and Knowledge Discovery*, 11(3), 550–557.
- Bishop, C. M. (2006). *Pattern recognition and machine learning*. (p. 738). New York: Springer.
- Burba, G., Schmidt, A., Scott, R. L., Nakai, T., Kathilankal, J., Fratini, G., Hanson, C., Law, B. E., McDermitt, D., Eckles, R., Furtaw, M., & Velgersdyk, M. (2011). Calculating CO_2 and H_2O eddy covariance fluxes from an enclosed gas analyzer using an instantaneous mixing ratio. *Global Change Biology*, 18, 385–399.
- Burden, F., & Winkler, D. (2009). Bayesian Regularization of Neural Networks. In D. J. Livingstone (Ed.), *Artificial neural networks: Methods and applications* (pp. 23–42). Totowa, NJ: Humana Press.
- Butenko, S., & Pardalos, P. M. (2014). *Numerical methods and optimization: An introduction*. (p. 412). London, New York: CRC Press, Taylor & Francis Group, Boca Raton.
- Creutzburg, M. K., Scheller, R. M., Lucash, M. S., Evers, L. B., LeDuc, S. D., & Johnson, M. G. (2016). Bioenergy harvest, climate change, and forest carbon in the Oregon Coast Range. *GCB Bioenergy*, 8, 357–370.
- Daly, C., Halbleib, M., Smith, J., Gibson, W., Doggett, M. K., Taylor, G. H., et al. (2008). Physiographically sensitive mapping of climatological temperature and precipitation across the conterminous United States. *International Journal of Climatology*, 28, 2031–2064.
- Dempsey, J., Plantinga, A., Kline, J. D., Lawler, J. J., Martinuzzi, S., Radeloff, V. C., et al. (2017). Effects of local land-use planning on development and disturbance in riparian areas. *Land Use Policy*, 60, 16–25.
- Dengel, S., Zona, D., Sachs, T., Aurela, M., Jammet, M., Parmentier, F. J. W., Oechel, W., & Vesala, T. (2013). Testing the applicability of neural networks as a gap-filling method using CH_4 flux data from high latitude wetlands. *Geosciences*, 10, 8185–8200. <http://dx.doi.org/10.5194/bg-10-8185-2013>.
- Foresee, F. D., & Hagan, M. T. (1997). Gauss-Newton approximation to Bayesian regularization. *IEEE Proceedings of IJCNN*, 1997, 1930–1935.
- Gaines, K. P., Meinzer, F. C., Duffy, C. J., Thomas, E. M., & Eissenstat, D. M. (2016). Rapid tree water transport and residence times in a Pennsylvania catchment. *Ecology*, 9, 1554–1565.
- Haykin, S. (1998). *Neural networks - a comprehensive foundation* (2nd ed.). (p. 842). Upper Saddle River, New Jersey, USA: Pearson Prentice Hall.
- Haykin, S. (2009). *Neural networks and learning machines* (3rd ed.). (p. 936). Upper Saddle River, New Jersey, USA: Pearson Prentice Hall.
- Hoover, D. L., & Rogers, B. M. (2016). Not all droughts are created equal: the impacts of interannual drought pattern and magnitude on grassland carbon cycling. *Global Change Biology*, 22, 1809–1820.
- Hudiburg, T. W., Luyssaert, S., Thornton, P. E., & Law, B. E. (2013). Interactive effects of environmental change and management strategies on regional forest carbon emissions. *Environmental Science and Technology*, 47, 13132–13140. <http://dx.doi.org/10.1021/es402903u>.
- Ito, A., Inatomi, M., Huntzinger, D. N., Schwalm, C., Michalak, A. M., et al. (2016). Decadal trends in the seasonal-cycle amplitude of terrestrial CO_2 exchange resulting from the ensemble of terrestrial biosphere models. *Tellus B*, 68. <http://dx.doi.org/10.3402/tellusb.v68.28968>.
- Liu, Y., Wang, Z., Liang, J., & Liu, X. (2008). Synchronization and state estimation for discrete-time complex networks with distributed delays. *IEEE Transactions on Systems, Man, and Cybernetics Part B: Cybernetics*, 38, 1314–1325.
- Liu, Y., Wang, Z., & Liu, X. (2006). Global exponential stability of generalized recurrent neural networks with discrete and distributed delays. *Neural Networks*, 19, 667–675.
- MacKay, D. J. C. (1992). Bayesian Interpolation. *Neural Computation*, 4, 415–447.
- Mahmood, R., Hubbard, K. G., & Carlson, C. (2004). Modification of growing season surface temperature records in the northern Great Plains due to land-use transformation: verification of modelling results and implication for global climate change. *International Journal of Climatology*, 24, 311–327.
- Marquardt, D. (1963). An Algorithm for Least-Squares Estimation of Nonlinear Parameters. *SIAM Journal on Applied Mathematics*, 11, 431–441.
- Meinzer, F. C., Brooks, J. R., Domec, J.-C., Gartner, B. L., Warren, J. M., Woodruff, D. R., et al. (2006). Dynamics of water transport and storage in conifers studied with deuterium and heat tracing techniques. *Plant, Cell and Environment*, 29, 105–114.
- Mekonnen, Z. A., Grant, R. F., & Schwalm, C. (2017). Carbon sources and sinks of North America as affected by major drought events during the past 30 years. *Agricultural and Forest Meteorology*, 244, 42–56.
- Menzer, O., Meiring, W., Kyriakidis, P. C., & McFadden, J. P. (2015). Annual sums of carbon dioxide exchange over a heterogeneous urban landscape through machine learning based gap-filling. *Atmospheric Environment*, 101, 312–327. <http://dx.doi.org/10.1016/j.atmosenv.2014.11.006>.

- Močkus, J., Tiesis, V., & Zilinskas, A. (1978). The application of Bayesian methods for seeking the extremum. In L. C. W. Dixon, & G. P. Szegő (Eds.), *Towards global optimization 2* (pp. 117–129). Amsterdam, New York, Oxford: North-Holland Publishing Company.
- OGWC (2017). Oregon Global Warming Commission - Biennial Report to the Legislature February 2017, 64.
- Oleson, K. W., & Lawrence, D. M., et al. (2013). Technical description of version 4.5 of the Community Land Model (CLM). NCAR Tech. Note NCAR/TN-5031STR, 422. <http://dx.doi.org/10.5065/D6RR1W7M>.
- Omernik, J. M. (1995). Ecoregions - a framework for environmental management. In W. S. Davis, & T. P. Simon (Eds.), *Biological assessment and criteria-tools for water resource planning and decision making* (pp. 49–62). Boca Raton, Florida: Lewis Publishers.
- Pan, Y., Chen, J. M., Birdsey, R., McCullough, K., He, L., & Deng, F. (2011). Age structure and disturbance legacy of North American forests. *Biogeosciences*, 8, 715–732.
- Papale, D., & Valentini, R. (2003). A new assessment of European forest carbon exchanges by eddy fluxes and artificial neural network spatialization. *Global Change Biology*, 9, 525–535.
- Peddinti, V., Povey, D., & Khudanpur, S. (2015). A time delay neural network architecture for efficient modeling of long temporal contexts. *Interspeech*, 2015, 3214–3218.
- Peichl, M., Sonnenag, O., Wohlfahrt, G., Flanagan, L. B., Baldocchi, D. D., Kiely, G., et al. (2013). Convergence of potential net ecosystem production among contrasting C-3 grasslands. *Ecology Letters*, 16, 502–512.
- Rahman, B., Blyuss, K. B., & Kyrychko, Y. N. (2015). Dynamics of neural systems with discrete and distributed time delays. *SIAM Journal on Applied Dynamical Systems*, 14, 2069–2095.
- Ruefenacht, B., Finco, M. V., Nelson, M. D., Czaplewski, R., Helmer, E. H., Blackard, J. A., et al. (2008). Conterminous U.S. and Alaska forest Type mapping using forest inventory and analysis data. *Photogrammetric Engineering and Remote Sensing*, 74, 1379–1388.
- Schmidt, A. C., Hanson, W., Chan, S., & Law, B. E. (2012). Empirical assessment of uncertainties of meteorological parameters and turbulent fluxes in the AmeriFlux network. *Journal of Geophysical Research*, 117(3), G04014. <http://dx.doi.org/10.1029/2012JG002100>.
- Schmidt, A., Hanson, C., Kathilankal, J., & Law, B. E. (2011). Classification and assessment of turbulent fluxes above ecosystems in North-America with self-organizing feature map networks. *Agricultural and Forest Meteorology*, 151, 508–520. <http://dx.doi.org/10.1016/j.agrformet.2010.12.009>.
- Schmidt, A., Law, B. E., Göckede, M., Hanson, C., Yang, Z., & Conley, S. (2016). Bayesian optimization of the Community Land Model simulated biosphere-atmosphere exchange using CO₂ observations from a dense tower network and aircraft campaigns over Oregon. *Earth Interactions*, 20. <http://dx.doi.org/10.1175/EI-D-16-0011.1>.
- Schmidt, A., Wrzesinsky, T., & Klemm, O. (2008). Gap filling and quality assessment of CO₂ and water vapour fluxes above an urban area with radial basis function neural networks. *Boundary-Layer Meteorology*, 126, 389–413.
- Schuepp, P. H., Leclerc, M. Y., MacPherson, J. I., & Desjardins, R. L. (1990). Footprint prediction of scalar fluxes from analytical solutions of the diffusion equation. *Boundary-Layer Meteorology*, 50, 355–373.
- Schwarz, P. A., Law, B. E., Williams, M., Irvine, J., Kurpius, M., & Moore, D. (2004). Climatic versus biotic constraints on carbon and water fluxes in seasonally drought-affected ponderosa pine ecosystems. *Global Biogeochemical Cycles*, 18, GB4007. <http://dx.doi.org/10.1029/2004GB002234>.
- Stoy, P. C., Katul, G. G., Siqueira, M. B. S., Juang, J.-Y., McCarthy, H. R., Kim, H.-S., Oishi, A. C., & Oren, R. (2005). Variability in netecosystem exchange from hourly to inter-annual time scales at adjacent pine and hardwood forests: a wavelet analysis. *Tree Physiology*, 25, 887–902.
- Taylor, K. E., Stouffer, R. J., & Meehl, G. A. (2012). An overview of CMIP5 and the experimental design. *Bulletin of the American Meteorological Society*, 485–498. <http://dx.doi.org/10.1175/BAMS-D-11-00094.1>.
- Thorson, T. D., Bryce, S. A., Lammers, D. A., Woods, A. J., Omernik, J. M., & Kagan, J., et al. (2003). Ecoregions of Oregon (color poster with map, descriptive text, summary tables, and photographs): Reston, Virginia, U.S. Geological Survey (map scale 1:1,500,000).
- Turner, D. P., Göckede, M., Law, B. E., Ritts, W. D., Cohen, W. B., Yang, Z., et al. (2011). Multiple constraints analysis of regional land-surface carbon flux. *Tellus B*, 63, 207–221.
- Turner, D. P., Ritts, W. D., Law, B. E., Cohen, W. B., Yang, Z., Hudiburg, T., et al. (2007). Scaling net ecosystem production and net biome production over a heterogeneous region in the western United States. *Biogeosciences*, 4, 597–612.
- USDA (2014). 2012 Census of Agriculture, Oregon State and County Data Vol. 1 Geographic Area series Part 37, 535.
- Vasquez, M., Milota, M., & Sinha, A. (2017). Quantifying environmental impacts of poplar biomass production in the U.S. Pacific Northwest. *Wood and Fiber Science*, 49, 193–205.
- Vickers, D., Thomas, C., Pettijohn, C., Martin, J. G., & Law, B. E. (2012). Five years of carbon fluxes and inherent water-use efficiency at two semi-arid pine forests with different disturbance histories. *Tellus B*, 64, 17159. <http://dx.doi.org/10.3402/tellusb.v64i0.17159>.
- Wagle, P., Xiao, X. M., Scott, R. L., Kolb, T. E., Cook, D. R., Brunsell, N., et al. (2015). Biophysical controls on carbon and water vapor fluxes across a grassland climatic gradient in the United States. *Agricultural and Forest Meteorology*, 214, 293–305.
- Waibel, A., Hanazawa, T., Hinton, G., Shikano, K., & Lang, K. J. (1989). Phoneme recognition using time-delay neural networks. *IEEE Transactions on Acoustics, Speech and Signal Processing*, 37, 328–339.
- Wang, Z., Liu, Y., & Liu, X. (2005). On global asymptotic stability of neural networks with discrete and distributed delays. *Physics Letters A*, 345, 299–308.
- Webb, E. K., Pearman, G. I., & Leuning, R. (1980). Correction of flux measurements for density effects due to heat and water vapour transfer. *Quarterly Journal of the Royal Meteorological Society*, 106, 85–100.
- Welp, L. R., Patra, P. K., Rödenbeck, C., Nemani, R., Bi, J., Piper, S. C., et al. (2016). Increasing summer net CO₂ uptake in high northern ecosystems inferred from atmospheric inversions and comparisons to remote-sensing NDVI. *Atmospheric Chemistry and Physics*, 16, 9047–9066. <http://dx.doi.org/10.5194/acp-16-9047-2016>.
- Wyngaard, J. C. (1990). Scalar fluxes in the planetary boundary layer-theory, modeling and measurement. *Boundary-Layer Meteorology*, 50, 49–75.